Stratification effects on the stability of columnar vortices on the f-plane

By P. G. POTYLITSIN and W. R. PELTIER

Department of Physics, University of Toronto, Toronto, Ontario, Canada M5S 1A7

We consider the stability with respect to three-dimensional perturbations of columnar vortices on the f-plane and as a function of the strength of a stabilizing density stratification parallel to the axis of the vortex. We seek to understand the dynamics of the processes through which such a vertically oriented barotropic vortex may be destabilized. As models of the basic vorticity distribution we consider both Kelvin–Helmholtz vortices in shear and 'Kida-like' vortices in strain. In the case of rotating unstratified flow, an isolated anticyclonic vortex column is shown to be strongly destabilized to three-dimensional perturbations by small values of the background rotation, while rapid rotation strongly stabilizes both anticyclonic and cyclonic columns, as expected on the basis of the Taylor–Proudman theorem. The dominant instability mechanism which drives the destruction of anticyclonic vortices in the presence of slow background rotation may be understood to constitute a three-dimensional inertial (centrifugal) instability. Through explicit analysis we show that sufficiently strong density stratification stabilizes the two-dimensional columnar structures to disruption by this and additional modes of instability that exist even in the absence of rotation. We furthermore demonstrate that there exists a second fundamental mode of instability in the presense of background rotation which affects only anticyclonic vortex columns whose cross-sections are elliptical. Only when the ellipticity of the vortex is sufficiently high does this mode dominate the centrifugal mode. The process whereby anticyclonic vortices may be selectively destroyed appears to provide a possible explanation of an asymmetry that is sometimes observed to be characteristic of the atmospheric von Kármán vortex streets that are observed in the lee of oceanic islands. The anticyclonic branch of the street often seems to be absent. More generally, the centrifugal mechanism for the selective destruction of anticyclones discussed herein very clearly explains a number of recent results obtained from both laboratory experiments and numerical simulations.

1. Introduction

Large-scale geophysical flows in the atmosphere and ocean are often dominated by horizontal motions in consequence of the strong influence of both rotation and stratification. In many cases, these quasi-two-dimensional flows also have embedded large-scale shear in the horizontal velocity which plays an essential role in the dynamics and which may give rise, through the barotropic instability mechanism, to the development of a two-dimensional train of vortices in which individual vortex axes are oriented vertically. The evolution of such vorticity distributions will not depend on the background rotation if the influence of rotation is considered from an f-plane perspective, nor on fluid stratification if the axis of rotation and density

gradient are parallel to the axis of the vortices in the developed two-dimensional flow. In such circumstances two-dimensional evolution of the flow may be studied through numerical solution of the two-dimensional nonlinear (barotropic) dynamical system which includes the influence of neither stratification nor background rotation.

If each vortex column in the array generated in this way is individually stable to arbitrary three-dimensional perturbations then even if the system were to be integrated forward in time using a fully three-dimensional model, the same history of flow evolution would be obtained as in a purely two-dimensional analysis. Our goal in this paper is to provide a detailed assessment of the circumstances in which such columnar structures would be expected to remain linearly stable and, when instability occurs, to characterize it fully.

The dynamical processes whereby such vortex columns may be formed are extremely interesting in themselves, and in this connection study of the evolution of a free shear layer has come to occupy a central position in theoretical hydrodynamics. Detailed analyses of the two-dimensional evolution of such shear flows have of course been abundantly discussed in the literature on mixing layers (e.g. Peltier, Halle & Clark 1978; Corcos & Sherman 1984; Klaassen & Peltier 1985*a*; Lesieur *et al.* 1988; Smyth & Peltier 1991, 1993) and through such analyses an idealized picture has emerged of the two-dimensional evolution of temporally growing homogeneous shear layers. Initially, the shear layer 'rolls up' to produce a train of discrete two-dimensional Kelvin–Helmholtz vortices whose wavelength is approximately seven times the initial depth of the layer. As the initial instability saturates, the subharmonic vortex pairing instability (e.g. Kelly 1967; Klaassen & Peltier 1985*b*) induces adjacent vortices to orbit one another and merge. As a result, each pair of vortices combines to produce a single vortex within which the primary vortices remain initially apparent, a structure which is then further transformed by diffusion into a single coherent vortex within a train of such structures (e.g. Smyth & Peltier 1993). The number of vortices is thereby reduced by a factor two and their scale is increased by the same factor. As a result, the effective thickness of the so-called mixing layer is doubled. This process then continues with further pairing events which lead to further broadening of the mixing layer (see Smyth & Peltier 1993 for an explicit example of the way in which continuous pairing drives the evolution of the mixing layer in a two-dimensional flow characterized by relatively large Reynolds number).

Only in very special circumstances, however, will such flows remain two-dimensional. Laboratory experiments that have been specifically designed to investigate the evolution of mixing layers (e.g. Wygnanski *et al.* 1979; Browand & Ho 1983) have demonstrated that fully three-dimensional motions invariably arise even though the flow may tend to remain quasi-two-dimensional on the scale of the large vortices. Recent experimental analyses of the evolution of barotropic vortices in a rotating environment (e.g. Kloosterziel & van Heijst 1991) have also demonstrated that the behaviour of initially two-dimensional cyclonic and anticyclonic vortices differs dramatically at moderate Rossby numbers, a fact that could be explained only by the presence of three-dimensional secondary circulations in the flow. (This conclusion follows immediately from the fact, previously noted, that two-dimensional vortices do not sense the background rotation as long as the influence of rotation is considered from an f-plane perspective and the axis of rotation is aligned with the axis of the vortices.) In order to develop a full understanding of experimental results such as those of Kloosterziel & van Heijst (1991), it is therefore essential to consider, from the most general possible perspective, the issue of vortex column stability.

Further analyses of this issue have recently been provided by Smyth & Peltier (1994) who focused upon the question of the linear stability of both non-rotating and rotating columnar vortices and by Dritschel & de la Torre Juarez (1996) who have analysed the linear stability of tall columnar vortices and the nonlinear development of such instabilities under the quasi-geostrophic approximation. Carnevale *et al.* (1997) have furthermore focused upon a model system close to that of Smyth & Peltier (1994) and investigated the way in which the three-dimensional centrifugal instability of the unstratified vortex column evolves at finite amplitude. In the additional analyses of this issue that form the core of the present paper, we will employ two alternative models of the vorticity distribution in the barotropic column in order to determine whether there might exist a finite (and hopefully small) set of universal mechanisms which control stability. Our analyses will pertain to the regime of moderately high Rossby number, for a reason that will become apparent below, and we will include the influence of density stratification parallel to the (vertical) axis of the vortex column. The first model that we will employ consists of an elliptical vortex in shear generated by a single stage of subharmonic merging, in a spatially periodic train of Kelvin–Helmholtz vortices, which takes place at finite but moderately large Reynolds number. The second model we will employ is that provided by a much simpler distribution similar to that introduced by Kida (e.g. see Moore & Saffman 1971; Kida 1981) which consists of an in general elliptical, horizontally uniform, patch of vorticity in a strain field. By comparing the results of analyses performed on these radically different structures, we will be testing the extent to which the mechanisms that lead to their destruction may be considered universal.

The theoretical techniques required to perform such analyses are by now well-known and have been described in detail by Pierrehumbert & Widnall (1982), Klaassen & Peltier (1985b, 1989, 1991) and Smyth & Peltier (1991, 1994). This methodology allows one to cast the linear three-dimensional perturbation equations into the form of a standard matrix eigenvalue problem whose solutions reveal the instability characteristics of the two-dimensional flow to three-dimensional perturbations. The initial analyses of the stability of an unstratified barotropic vortex column on the f-plane performed by Smyth & Peltier (1994) clearly demonstrated the existence of a three-dimensional centrifugal instability to which anticyclonic vortex columns are subject in circumstances in which the Rossby number is moderate (i.e. of order unity). This mechanism arises in flow with relatively weak background rotation which tends to reduce the absolute vorticity of an anticyclonic vortex to a value near zero and, thereby, to destabilize the flow. The conditions in which three-dimensional centrifugal instability arises are extremely interesting since, although the necessary condition for instability due to Rayleigh does successfully predict the spatial region within which the instability develops, detailed analysis is required to determine the prefered axial scale. A central motivation for the work to be described below is to understand whether this mechanism (or, in fact, the family of mechanisms, as we will see) may play an important role in circumstances that are geophysically interesting.

In addressing the issue of geophysical relevance, it is clearly important to understand the extent to which this mechanism for the selective destruction of anticyclonic vortex columns may be sensitive to the influence of density stratification parallel to the axis of the column. If infinitesimally weak stratification were to suffice to quell the instability, for example, then the mechanism might be expected to be less relevant to the understanding of atmospheric and oceanographic phenomenology than would otherwise be the case. In figure 1 we present an example of one class of observation to which the analyses to be reported herein may be applied. This shows satellite
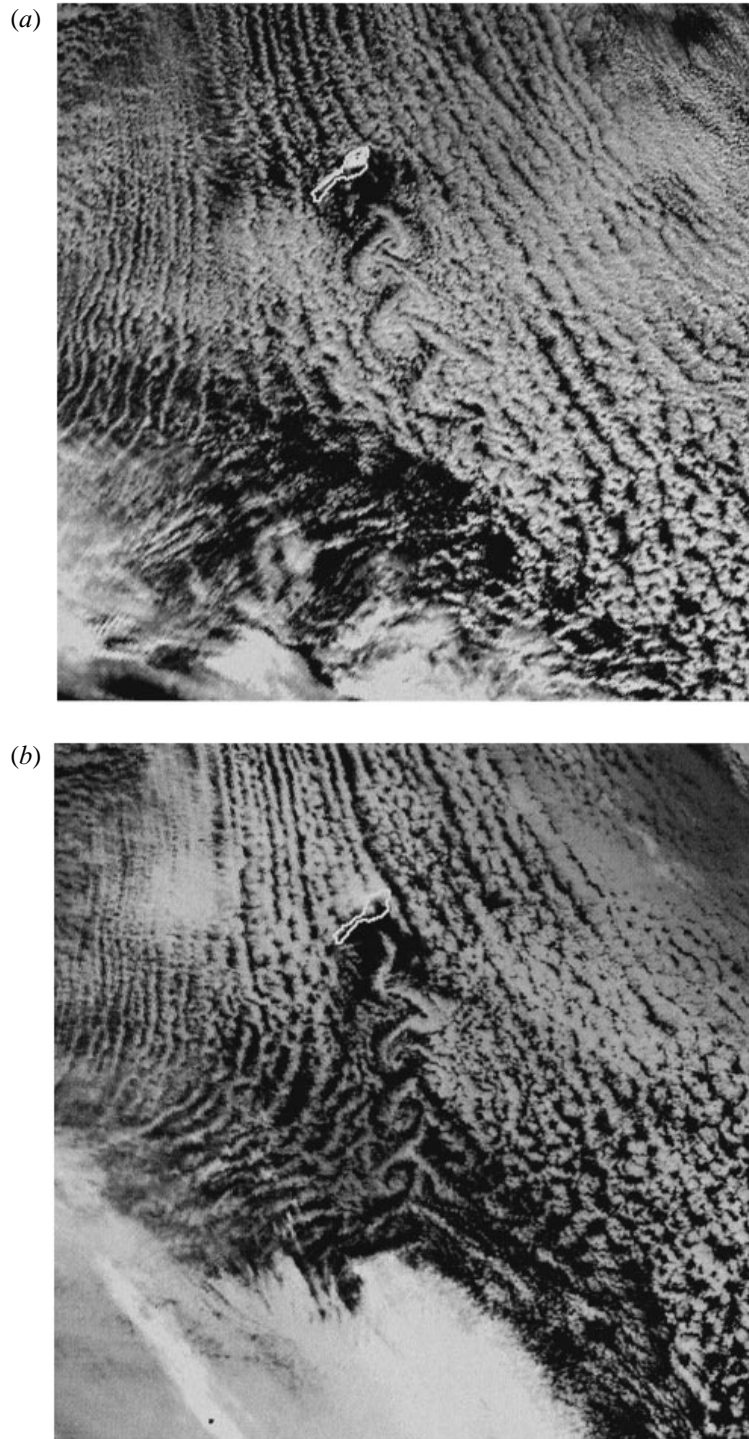
FIGURE 1. (*a*) Symmetric and (*b*) asymmetric von Kármán vortex streets generated in the lee of the island of Jan Mayen (71° N, 8.5° W) which is 55 km in length. The highest peak, a cone at the northeast end, is 2277 m. The airflow is from the north (top) and blocked by the island, outlined in white.

photographs of the von Kármán vortex streets that are very often observed to develop in the lee of Jan Mayen island (71° N, 8.5° W). In (*a*) the street is of conventional form with both the anticyclonic and cyclonic branches equally well developed. This is in contrast to (*b*) in which the anticyclonic vortices do not appear. Since the environment in which these structures develop is stratified in the vertical and since it is reasonable to expect that the influence of such stratification will be to reduce the intensity of a three-dimensional instability, we might imagine that the anticyclones in the street would be more likely to be destroyed when the vertical stability is weak than when it is strong. The circumstances in which the issue of the stability of a stratified vortex column arises, however, very clearly transcend this specific phenomenon and might be seen more generally to arise in the broad context of rotating stratified turbulence. It may well be, in fact, that the broken symmetry evident in figure 1 is due to a process other than that to be described herein. Perhaps the most definitive demonstration of the existence of a mechanism that selectively destroys anticyclones under conditions of moderately high Rossby number is that observed in the numerical simulations of Bartello, Metais & Lesieur (1994) and in the previously mentioned laboratory experiments by Kloosterziel & van Heijst (1991). Our focus in what follows will therefore be on the central issue of the determinants of barotropic vortex column stability rather than upon any particular circumstance in which the consequences of such stability/instability become manifest.

In the next section of the paper we will review, and considerably extend, the theoretical methods that we have previously developed to enable detailed investigation of the broad class of problems in which the issue of the stability of two-dimensional flow to arbitrary three-dimensional perturbations arises. Section 3 is devoted to the presentation and analysis of the results that we have obtained by applying this theoretical structure to analyse the stability of the elliptical vortex column in shear, whereas §4 is devoted to a parallel discussion of the 'Kida-like' vortex in strain. Conclusions are summarized in §5.

2. Methodology

In this section, the analytical and numerical methods that have been developed to simulate the evolution of two-dimensional nonlinear vortices in shear flow and to test the linear instability characteristics of these flows to three-dimensional perturbations will be presented. The two-dimensional nonlinear model has been adapted from the previous studies of mixing layers by Smyth & Peltier (1991, 1993). We will also discuss the 'Kida-like' model vortex in order to contrast it to the elliptical vortex that is generated by pairing in a train of Kelvin–Helmholtz waves. The three-dimensional linear stability methods developed originally by Klaassen & Peltier (1985*b*, 1989, 1991) and Smyth & Peltier (1989, 1991, 1994) are also extended to incorporate the influence of a stable density stratification parallel to the axis of a two-dimensional vortex.

2.1. *Two-dimensional vortical coherent structures*

As mentioned previously, the first model of a barotropic columnar vortex to be employed herein will be one for an elliptical vortex generated by the pairing interaction in a free shear layer. The initial state of the shear layer is shown in figure 2. The geophysically unconventional labelling of the coordinate axes has been employed to maintain consistency with previous analyses in which the coordinate direction normal to the mean flow was taken to be the z-direction. If the angular velocity Ω
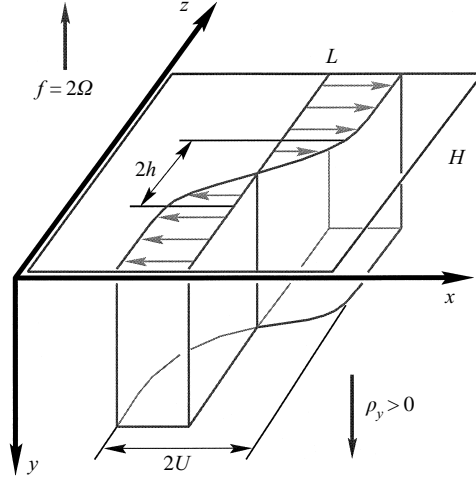
FIGURE 2. The coordinate system and the initial state of the shear flow. The system rotates along the y-axis with the angular velocity $\Omega = f/2$, where f is the Coriolis parameter. The density gradient is parallel to the y-axis. L and H are the x- and z-dimensions of the computational domain. U and h are the velocity and length scales of the shear layer which were used for non-dimensionalization of the equations of motion.

is taken to represent the Earth's rotation, then our x-, y- and z-axes would denote the zonal, vertically downwards and meridional directions, respectively. At the initial instant of time, we may assume the flow to consist of a two-dimensional shear layer with hyperbolic-tangent velocity profile $U(z) = U_0 \tanh(z/h)$, where U_0 and $2h$ are the characteristic velocity and depth of the shear layer respectively. The coordinate system rotates with background angular velocity $\Omega = f/2$, where f is the usual Coriolis parameter that appears in both oceanographic and atmospheric contexts. In this basic state we will assume that density increases in the y-direction and that the gravitational body force in this direction is balanced hydrostatically. The instability of this basic state is evolved in a domain with x- and z-dimensions of L and H respectively.

In this domain the flow satisfies the Navier–Stokes and continuity equations for two-dimensional incompressible flow which, on the f-plane, take the form

$$\frac{\partial \boldsymbol{U}}{\partial t} + (\boldsymbol{U} \cdot \nabla)\boldsymbol{U} = -\frac{1}{\rho}\nabla p + \nu\nabla^2 \boldsymbol{U} - \boldsymbol{f} \times \boldsymbol{U} + \boldsymbol{g}, \tag{2.1a}$$

$$\nabla \cdot \boldsymbol{U} = 0, \tag{2.1b}$$

in which the velocity $\boldsymbol{U} = (U, 0, W)$, the Coriolis parameter $\boldsymbol{f} = (0, -2\Omega, 0)$, p is the pressure, ν is the kinematic viscosity, $\boldsymbol{g} = (0, g, 0)$ is the gravitational acceleration and t denotes time. The vorticity $\boldsymbol{\omega}$ and the stream function ψ for this two-dimensional flow are defined in the usual way according to

$$\boldsymbol{\omega} = \nabla \times \boldsymbol{U} \quad \Longrightarrow \quad \boldsymbol{\omega} = (0, \omega, 0), \quad \omega = \frac{\partial U}{\partial z} - \frac{\partial W}{\partial x}, \tag{2.2a}$$

$$\boldsymbol{U} = \nabla \times (\psi \boldsymbol{j}) \quad \Longrightarrow \quad U = -\frac{\partial \psi}{\partial z}, \quad W = \frac{\partial \psi}{\partial x}. \tag{2.2b}$$

In terms of these dynamical variables the vector coupled system (2.1) reduces to the

following pair of partial differential equations in the scalar fields ω and ψ:

$$\frac{\partial \omega}{\partial t} = \frac{\partial \omega}{\partial x}\frac{\partial \psi}{\partial z} - \frac{\partial \omega}{\partial z}\frac{\partial \psi}{\partial x} + \frac{1}{Re}\nabla^2\omega, \qquad (2.3a)$$

$$\nabla^2\psi = -\omega, \qquad (2.3b)$$

in which $Re = hU_0/v$ is the Reynolds number. Note that in writing (2.3) the above system has been non-dimensionalized in terms of the length scale h which equals half the total depth of the shear layer (see figure 2) and the velocity scale U_0 which equals half the total change in velocity across the shear layer. Note also that system (2.3) for the vorticity and the stream function of the two-dimensional flow depends neither upon the vertical stratification nor the background rotation. The physical influence of both rotation and stratification affects only three-dimensional motion and, therefore, the barotropic dynamics is unsensitive to their influence. The vertical stratification may be characterized by the buoyancy frequency $N^2 = (g/\rho)\,\mathrm{d}\rho/\mathrm{d}y$ in which g is the gravitational acceleration (assumed constant) and ρ denotes the density field, whereas the background rotation Ω is characterized by the Coriolis parameter $f = 2\Omega$.

In the z-direction we solve (2.3) subject to boundary conditions

$$\omega = \psi = 0 \qquad \text{on} \quad z = 0, H. \qquad (2.4)$$

In the streamwise direction we assume the flow to be periodic with fundamental wavenumber α such that $\alpha = 2\pi/L$. We may therefore expand the vorticity ω and stream function ψ in terms of the following Fourier series decompositions:

$$\omega(x, z, t) = \sum_{v=-N}^{N} \omega_v(z, t)\mathrm{e}^{\mathrm{i}v\alpha x}, \quad \psi(x, z, t) = \sum_{v=-N}^{N} \psi_v(z, t)\mathrm{e}^{\mathrm{i}v\alpha x}. \qquad (2.5)$$

Note also that $\omega_v = \omega_{-v}^*$ and $\psi_v = \psi_{-v}^*$ (in which the superscript $*$ denotes complex conjugation) since the vorticity ω and the stream function ψ are real-valued functions, and it is therefore unnecessary to compute coefficients in these expansions with negative indices. Solutions are constructed using well-established procedures (e.g. see Smyth & Peltier 1991)

A typical result obtained through application of this two-dimensional model to solve the initial value problem for the barotropic evolution of the free shear layer is shown in figure 3. For the purpose of this analysis the basic-state profile of vorticity was assumed to be $\omega(z) = 1/\cosh^2 z$ and this was perturbed at $t = 0$ by the superposition of a component consisting of small-amplitude white noise and a harmonic disturbance with wavelength equal to half the length of the domain. The length of the domain was set equal to twice the wavelength of the fastest growing mode of linear stability theory and the structure of the harmonic component of the perturbation to the parallel flow was determined by the eigenfunction of this mode. For the purpose of this analysis the Reynolds number was set to 300, typical for most small-scale shear flows generated in the laboratory. The x- and z-dimensions of the domain were chosen to be $L = 28$ and $H = 40$, respectively, in non-dimensional units. To fully resolve details of the flow the number of points in the z-direction of the domain, M, and the number of spectral modes, N, in equations (2.5) were set to 256 and 64 respectively. In figure 3 the evolution of the barotropic vorticity field is shown in a reduced portion of the domain of length $L = 28$ and width 28 whereas the full width $H = 40$.

The individual frames in figure 3 illustrate the vorticity distribution at a sequence of non-dimensional times t. At the instant of time $t = 20$, the initially unstable
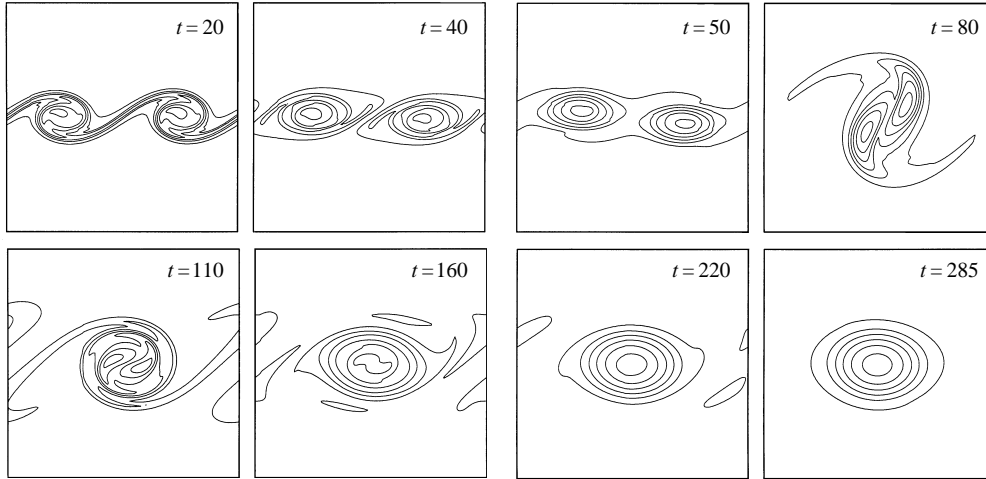
FIGURE 3. The evolution with time of vorticity fields for the two-dimensional hyperbolic-tangent shear layer in the domain chosen so as to accommodate two wavelengths of the primary Kelvin–Helmholtz instability. The Reynolds number $Re = 300$. Non-dimensional time is shown in the pictures. The visual non-dimensional size of the domain is 28×28.

shear layer is observed to have produced a train of two vortices with wavelength equal to half the length of the domain. As one may observe, the Kelvin–Helmholtz instability grows rapidly and the subharmonic of the primary disturbance is visible by $t = 50$. From $t = 50$ to $t = 110$ the vortices are undergoing the subharmonic pairing interaction and by time $t = 110$ a single vortex has begun to emerge within which the primary 'parent' vortices still remain apparent. This structure is observed to be converted into a single elliptical vortex by $t = 285$. If the numerical domain were not restricted in length then a second pairing interaction would begin at this time, but the periodic boundary conditions prevent further merging and the numerical simulation is thus terminated at this point. This vortex is of course implicitly part of a train of elliptical vortices which is similar in form to the analytical solution of the Euler equations obtained by Stuart (1967) when the free parameter in his model is appropriately chosen. The evolution of the vortex in this phase of its evolution is characterized by a slow viscous diffusion of vorticity out of the core and by a weak nutation due to the influence of the neighbouring vortices.

In what follows we will use the vorticity distribution in the last phase of figure 3 as the first model of the cross-section of a barotropic columnar vortex to be employed as basic state in our analyses of instability.

The second model of the vorticity distribution in the columnar vortex that we will use for comparison purposes is similar to the Kida model. The Kida model has often been invoked as a simple model of a vortex in the field of distant vortices. The model has also been successfully applied to understanding the Great Dark Spot of the planet Neptune (Polvani *et al.* 1990). The Kida vortex (Kida 1981; Moore & Saffman 1975) is a two-dimensional elliptical patch of vorticity superimposed on a constant uniform irrotational background strain field in inviscid incompressible flow. The total flow is in general time-dependent and the elliptical vortex undergoes both nutation and rotation, although some steady solutions also exist (Moore & Saffman 1975). The x- and z-velocity components of the background straining flow may be written $U = -ez$ and $W = -ex$ respectively, in which e is a constant rate of strain.
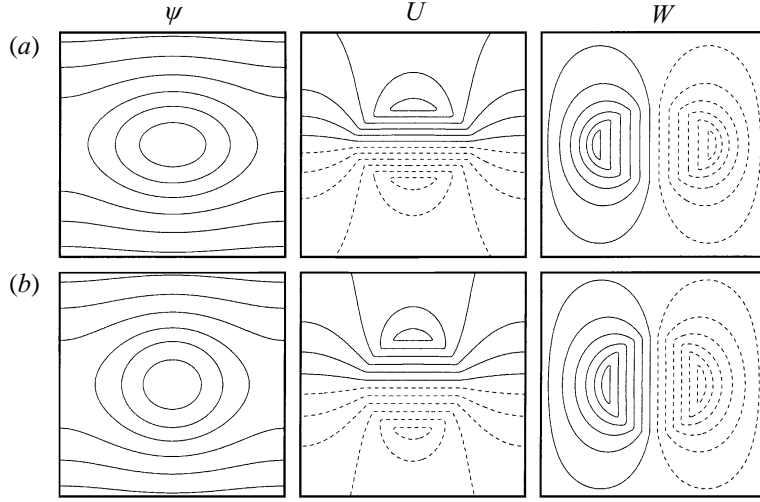
FIGURE 4. The two-dimensional stream function ψ, x-component of velocity U and z-component of velocity W in the (X, Z)-plane for the Kida-like model (*a*) with the elliptical background vorticity distribution presented in figure 6(*b*), and (*b*) with the circular background vorticity distribution presented in figure 6(*c*).

The total flow is then characterized by uniform vorticity $\omega = \omega_0$ inside and $\omega = 0$ outside the ellipse. The model thus corresponds to an isolated elliptical vortex in an irrotational straining field of infinite extent, and is not spatially periodic. The three-dimensional stability theory to be employed herein to analyse the instability of the previously discussed Kelvin–Helmholtz columnar vortex, however, assumes periodic boundary conditions in the streamwise (x-) direction. Therefore, if we were to employ the Kida vorticity distribution in the columnar vortex, a discrepancy would arise in the boundary conditions between those satisfied by the two-dimensional basic-state flow and those imposed for the purpose of the three-dimensional stability analysis. In order to avoid this problem, we design a 'Kida-like' model of the basic-state columnar vortex as follows. We begin by defining an, in general, elliptical vorticity distribution with the ellipticity as a free parameter and with the vorticity constant within the ellipse. We then solve $\nabla^2\psi = -\omega$ (see equation (2.3)) numerically in a computational domain subject to periodic boundary conditions in the x-direction and boundary conditions (2.4) in the z-direction. As a result, we implicitly obtain a periodic train of elliptical columnar vortices with constant core vorticity ω_0 in an irrotational strain field. Examples of such solutions for the initial distribution of vorticity shown on figure 6(*b*) (elliptical) and figure 6(*c*) (circular) are presented in figure 4 in terms of the stream function and velocity field components U and W.

2.2. *Three-dimensional stability theory for two-dimensional coherent vortical structures in stratified rotating flow*

We turn next to a discussion of the mathematical methods to be employed in the three-dimensional linear stability analyses of the two models of a columnar vortex described in the last section. The techniques required in the present context should be viewed as an extension of those previously elaborated by Klaassen & Peltier (1985*b*, 1989, 1991) and by Smyth & Peltier (1989, 1991, 1994). Further extensions of these procedures will be required for present purposes to incorporate the influence of density stratification parallel to the axis of the two-dimensional vortex.

These extensions to existing theory will be based upon the Navier–Stokes equation, the continuity equation and the equation of state for three-dimensional incompressible vertically stratified and rotating flow in the Boussinesq and f-plane approximations. Subject to these approximations, the appropriate field equations are

$$\boldsymbol{U}_t + (\boldsymbol{U} \cdot \nabla)\boldsymbol{U} = -\frac{1}{\rho}\nabla p + \nu\nabla^2\boldsymbol{U} - \boldsymbol{f} \times \boldsymbol{U} + \frac{\rho}{\rho_0}\boldsymbol{g}, \tag{2.6a}$$

$$\nabla \cdot \boldsymbol{U} = 0, \tag{2.6b}$$

$$\frac{\mathrm{D}\rho}{\mathrm{D}t} = 0, \tag{2.6c}$$

in which ρ is the density of the fluid and ρ_0 a reference density. The innovation with respect to previous work to be developed in what follows involves the addition of a stabilizing density stratification parallel to the axis of rotation (y-axis). Note that the two-dimensional basic-state flows described in the previous subsection are independent of the spanwise coordinate y. Assuming, without loss of generality, that three-dimensional perturbations vary sinusoidally in the spanwise direction parallel to the axis of the vortex column, we may expand the three-dimensional fields as the sum of the basic-state barotropic vortex plus a three-dimensional perturbation as:

$$\Phi(x, y, z, t) = \tilde{\Phi}(x, z, t) + \hat{\Phi}(x, z, t)\mathrm{e}^{\mathrm{i}dy}, \quad \hat{\Phi}(x, z, t) \ll \tilde{\Phi}(x, z, t) \tag{2.7}$$

in which d is the spanwise wavenumber; Φ represents pressure or any component of the velocity vector for the three-dimensional flow (note also that density perturbations are represented as $\rho(x, y, z, t) = \tilde{\rho}(y) + \hat{\rho}(x, z, t)\mathrm{e}^{\mathrm{i}dy}$), $\tilde{\Phi}$ denotes the corresponding fields of the two-dimensional basic state and $\hat{\Phi}$ represents the complex amplitude of the perturbation to the basic state. This amplitude, according to (2.7), is assumed to constitute a small perturbation to the basic-state flow.

Substituting these expansions into (2.6) and linearizing in the perturbations, we obtain the following non-dimensional set of linear partial differential equations that governs the fate of small-amplitude fluctuations:

$$\hat{u}_t = -\tilde{U}\hat{u}_x - \tilde{U}_x\hat{u} - \tilde{W}\hat{u}_z - \tilde{U}_z\hat{w} - \hat{p}_x + \frac{1}{Re}\Delta\hat{u} + \frac{1}{Ro}\hat{w}, \tag{2.8a}$$

$$\hat{v}_t = -\tilde{U}\hat{v}_x - \tilde{W}\hat{v}_z - \mathrm{i}d\hat{p} + \frac{1}{Re}\Delta\hat{v} + \frac{1}{Fr^2}\hat{\rho}, \tag{2.8b}$$

$$\hat{w}_t = -\tilde{U}\hat{w}_x - \tilde{W}_x\hat{u} - \tilde{W}\hat{w}_z - \tilde{W}_z\hat{w} - \hat{p}_z + \frac{1}{Re}\Delta\hat{w} - \frac{1}{Ro}\hat{u}, \tag{2.8c}$$

$$\hat{u}_x + \mathrm{i}d\hat{v} + \hat{w}_z = 0, \tag{2.8d}$$

$$\hat{\rho}_t = -\tilde{U}\hat{\rho}_x - \hat{v} - \tilde{W}\hat{\rho}_z, \tag{2.8e}$$

in which $\Delta\hat{\Phi} \equiv \hat{\Phi}_{xx} + \hat{\Phi}_{zz} - d^2\hat{\Phi}$, the Reynolds number $Re = hU_0/\nu$, the Rossby number $Ro = U_0/fh$ and the Froude number $Fr = U_0/(Nh)$. Note that for the purpose of non-dimensionalization the velocity scale U_0 is taken to be equal to one-half the total change in velocity across the shear layer as previously (see figure 2), the length scale h is taken to be equal to one-half of the width of the shear layer, the scale for the pressure perturbation is taken to be $[\hat{p}] = \rho_0 U_0^2$ and the scale for the density perturbation to be $[\hat{\rho}] = \rho_0 hN^2/g$.

The first three equations in (2.8) may be combined to obtain an equation for the three-dimensional divergence of the perturbation velocity which reduces to a

diagnostic equation for the pressure that incorporates the constraint of continuity as

$$\Delta\hat{p} = -\frac{1}{Ro}(\hat{u}_z - \hat{w}_z) + \frac{\mathrm{i}d}{Fr^2}\hat{\rho} - 2(\tilde{U}_x\hat{u}_x + \tilde{U}_z\hat{w}_x + \tilde{W}_x\hat{u}_z + \tilde{W}_z\hat{w}_z). \qquad (2.9)$$

To solve the set of stability equations (2.8) we restrict attention to the same domain $0 \leqslant x \leqslant L$, $0 \leqslant z \leqslant H$ as that on which the barotropic vorticity equation was solved to obtain our models of a barotropic columnar vortex. The boundary conditions in the z-direction that must be satisfied by the amplitudes of the three-dimensional perturbations $\hat{\Phi}$ are, explicitly, on $z = 0, H$:

$$\hat{u}_z = \hat{v}_z = \hat{w} = \hat{p}_z = \hat{\rho} = 0. \qquad (2.10)$$

Since the boundary conditions in the x-direction are periodic we may apply the Galerkin method to represent the perturbation fields. Specifically the x- and z-dependences of the perturbation fields are represented spectrally by introducing the following complete set of orthogonal functions selected so that the boundary conditions for the dependent variables are satisfied automatically:

$$F_{\lambda v} = \mathrm{e}^{\mathrm{i}\lambda\alpha x}\cos\frac{v\pi}{H}z, \quad G_{\lambda v} = \mathrm{e}^{\mathrm{i}\lambda\alpha x}\sin\frac{v\pi}{H}z \qquad (2.11a,b)$$

In terms of these orthogonal functions, the velocity, density and pressure perturbation fields may be expanded as:

$$\begin{pmatrix} \hat{u} \\ \hat{v} \\ \hat{p} \end{pmatrix} = \begin{pmatrix} u_{\lambda v} \\ v_{\lambda v} \\ p_{\lambda v} \end{pmatrix} F_{\lambda v}, \qquad \begin{pmatrix} \hat{w} \\ \hat{\rho} \end{pmatrix} = \begin{pmatrix} w_{\lambda v} \\ \rho_{\lambda v} \end{pmatrix} G_{\lambda v}, \qquad (2.12)$$

in which it is understood that repeated indices are to be summed over.

It is worth noting that if the solutions of interest had appreciable amplitude near the boundaries $z = 0, H$, the boundary condition for $\hat{p}$ would need to be replaced by $\hat{p}_z = -Ro^{-1}\hat{u}$ and the boundary condition for $\hat{\rho}$ would be $\hat{\rho}_t = -U\hat{\rho}_x - \hat{v}$. It would therefore follow, in the case in which f is non-zero, that the pressure perturbation would be expanded in terms of the $G_{\lambda v}$ rather than $F_{\lambda v}$ to take into account the Coriolis force. Similarly the density perturbation would be represented in terms of the $F_{\lambda v}$ rather than $G_{\lambda v}$ to take proper account of the vertical motion. Therefore, coefficients of the stability matrix $\boldsymbol{A}_{\lambda v}^{\kappa\mu}(t)$ (see below) would have slightly different forms. In the present application, the eigenfunctions of the stability problem for modes that are of interest to us are localized far from the rigid boundaries and there is no appreciable difference between the results obtained using the two different sets of boundary conditions on $z = 0, H$, namely $\hat{p}_z = 0$, $\hat{\rho} = 0$ or $\hat{p}_z = -Ro^{-1}\hat{u}$, $\hat{\rho}_t = U\hat{\rho}_x - \hat{v}$.

The procedure for the construction of solutions is completed by substituting (2.12) into (2.8) and (2.9) and computing the inner products $\langle F_{\kappa\mu}^*\bullet\rangle$ or $\langle G_{\kappa\mu}^*\bullet\rangle$ with each equation, where $\bullet$ represents any equation of the set (2.8) and (2.9) and in which the symbol $*$ denotes complex-conjugation. This inner product is defined as

$$\langle\star\rangle = \frac{\alpha}{\pi H}\int_0^{2\pi/\alpha}\mathrm{d}x\int_0^H \star\,\mathrm{d}z \qquad (2.13)$$

The pressure may clearly be eliminated from the system (2.8) using the diagnostic equation (2.9). The remaining equations can be reduced to a set of linear ordinary differential equations. In following this procedure it is important to note that

$$\langle F_{\kappa\mu}^*F_{\lambda v}\rangle = \delta_{\lambda v}\delta_{\mu v}(1 + \delta_{\mu 0}) \quad \text{and} \quad \langle G_{\kappa\mu}^*G_{\lambda v}\rangle = \delta_{\lambda v}\delta_{\mu v}(1 - \delta_{\mu 0}).$$

These operations reduce (2.8) to the following matrix form:

$$\frac{\mathrm{d}}{\mathrm{d}t}\begin{pmatrix} u_{\kappa\mu} \\ v_{\kappa\mu} \\ w_{\kappa\mu} \\ \rho_{\kappa\mu} \end{pmatrix} = \boldsymbol{A}_{\lambda\nu}^{\kappa\mu}(t)\begin{pmatrix} u_{\lambda\nu} \\ v_{\lambda\nu} \\ w_{\lambda\nu} \\ \rho_{\lambda\nu} \end{pmatrix} \tag{2.14}$$

in which $\boldsymbol{A}_{\lambda\nu}^{\kappa\mu}(t)$ is a complex matrix whose time-dependence reflects the time-dependence of the two-dimensional background flow. It is defined as

$$\boldsymbol{A}_{\lambda\nu}^{\kappa\mu}(t) = \begin{pmatrix} \langle UU\rangle_{\lambda\nu}^{\kappa\mu} & 0 & \langle UW\rangle_{\lambda\nu}^{\kappa\mu} & \langle U\rho\rangle_{\lambda\nu}^{\kappa\mu} \\ \langle VU\rangle_{\lambda\nu}^{\kappa\mu} & \langle VV\rangle_{\lambda\nu}^{\kappa\mu} & \langle VW\rangle_{\lambda\nu}^{\kappa\mu} & \langle V\rho\rangle_{\lambda\nu}^{\kappa\mu} \\ \langle WU\rangle_{\lambda\nu}^{\kappa\mu} & 0 & \langle WW\rangle_{\lambda\nu}^{\kappa\mu} & \langle W\rho\rangle_{\lambda\nu}^{\kappa\mu} \\ 0 & \langle \rho V\rangle_{\lambda\nu}^{\kappa\mu} & 0 & \langle \rho\rho\rangle_{\lambda\nu}^{\kappa\mu} \end{pmatrix}. \tag{2.15}$$

Explicit expressions for the four-dimensional arrays of interaction coefficients $\langle UU\rangle_{\lambda\nu}^{\kappa\mu}$, $\langle UV\rangle_{\lambda\nu}^{\kappa\mu}$, etc. will be found in the Appendix.

It is possible to decrease the size of the matrix $\boldsymbol{A}_{\lambda\nu}^{\kappa\mu}(t)$, and therefore to decrease the machine memory and CPU time required for the numerical calculations, by employing the following procedures. From the continuity equation in the system (2.8) one may obtain a diagnostic equation connecting $u_{\lambda\nu}$, $v_{\lambda\nu}$ and $w_{\lambda\nu}$ in the form

$$v_{\lambda\nu} = -\frac{\lambda a}{d} u_{\lambda\nu} + \frac{\mathrm{i}D_\nu}{d} w_{\lambda\nu} \tag{2.16}$$

in which $D_\nu = \nu\pi/H$. Substituting this diagnostic equation into the equation for $\rho_{\kappa\mu}$ in system (2.14) one may slightly modify its form by eliminating the dependence on $v_{\lambda\nu}$. Following this operation the matrix $\boldsymbol{A}_{\lambda\nu}^{\kappa\mu}(t)$ becomes

$$\boldsymbol{A}_{\lambda\nu}^{\kappa\mu}(t) = \begin{pmatrix} \langle UU\rangle_{\lambda\nu}^{\kappa\mu} & 0 & \langle UW\rangle_{\lambda\nu}^{\kappa\mu} & \langle U\rho\rangle_{\lambda\nu}^{\kappa\mu} \\ \langle VU\rangle_{\lambda\nu}^{\kappa\mu} & \langle VV\rangle_{\lambda\nu}^{\kappa\mu} & \langle VW\rangle_{\lambda\nu}^{\kappa\mu} & \langle V\rho\rangle_{\lambda\nu}^{\kappa\mu} \\ \langle WU\rangle_{\lambda\nu}^{\kappa\mu} & 0 & \langle WW\rangle_{\lambda\nu}^{\kappa\mu} & \langle W\rho\rangle_{\lambda\nu}^{\kappa\mu} \\ \langle \rho U\rangle_{\lambda\nu}^{\kappa\mu} & 0 & \langle \rho W\rangle_{\lambda\nu}^{\kappa\mu} & \langle \rho\rho\rangle_{\lambda\nu}^{\kappa\mu} \end{pmatrix}. \tag{2.17}$$

It is now obvious that the set of equations for $v_{\kappa\mu}$ decouples from the system and in order to further reduce the dimension of the matrix one may remove these equations from (2.17) because $u_{\kappa\mu}$, $w_{\kappa\mu}$ and $\rho_{\kappa\mu}$ do not depend on $v_{\lambda\nu}$. Applying this further reduction leads finally to the following set of ordinary differential equations:

$$\frac{\mathrm{d}}{\mathrm{d}t}\begin{pmatrix} u_{\kappa\mu} \\ w_{\kappa\mu} \\ \rho_{\kappa\mu} \end{pmatrix} = \begin{pmatrix} \langle UU\rangle_{\lambda\nu}^{\kappa\mu} & \langle UW\rangle_{\lambda\nu}^{\kappa\mu} & \langle U\rho\rangle_{\lambda\nu}^{\kappa\mu} \\ \langle WU\rangle_{\lambda\nu}^{\kappa\mu} & \langle WW\rangle_{\lambda\nu}^{\kappa\mu} & \langle W\rho\rangle_{\lambda\nu}^{\kappa\mu} \\ \langle \rho U\rangle_{\lambda\nu}^{\kappa\mu} & \langle \rho W\rangle_{\lambda\nu}^{\kappa\mu} & \langle \rho\rho\rangle_{\lambda\nu}^{\kappa\mu} \end{pmatrix}\begin{pmatrix} u_{\lambda\nu} \\ w_{\lambda\nu} \\ \rho_{\lambda\nu} \end{pmatrix}. \tag{2.18}$$

One may further reduce the stability matrix $\boldsymbol{A}_w \lambda\nu^{\kappa\mu}(t)$ by noting that the elements $\omega_{\lambda\nu(\nu=0)}$ and $\rho_{\lambda\nu(\nu=0)}$ influence neither the z-component of the velocity nor the density perturbation field because $G_{\lambda\nu(\nu=0)} \equiv 0$. Therefore, one may put $\omega_{\lambda\nu(\nu=0)} \equiv 0$ and $\rho_{\lambda\nu(\nu=0)} \equiv 0$ and exclude coefficients $\langle WU\rangle_{\lambda\nu}^{\kappa 0}$, $\langle WW\rangle_{\lambda\nu}^{\kappa 0}$, $\langle W\rho\rangle_{\lambda\nu}^{\kappa 0}$ and $\langle UW\rangle_{\lambda 0}^{\kappa\mu}$, $\langle WW\rangle_{\lambda 0}^{\kappa\mu}$, $\langle \rho W\rangle_{\lambda 0}^{\kappa\mu}$ as well as $\langle \rho U\rangle_{\lambda\nu}^{\kappa 0}$, $\langle \rho W\rangle_{\lambda\nu}^{\kappa 0}$, $\langle \rho\rho\rangle_{\lambda\nu}^{\kappa 0}$ and $\langle U\rho\rangle_{\lambda 0}^{\kappa\mu}$, $\langle W\rho\rangle_{\lambda 0}^{\kappa\mu}$, $\langle \rho\rho\rangle_{\lambda 0}^{\kappa\mu}$ from the matrix $\boldsymbol{A}_{\lambda\nu}^{\kappa\mu}(t)$ and this once again leads to a further substantial decrease of the dimension of the matrix. Note that in the case of unstratified flow ($Fr^{-2} = 0$) equation (2.18)

reduces to

$$\frac{\mathrm{d}}{\mathrm{d}t} \left(\begin{array}{c} u_{\kappa\mu} \\ w_{\kappa\mu} \end{array} \right) = \left(\begin{array}{cc} \langle UU \rangle_{\lambda\nu}^{\kappa\mu} & \langle UW \rangle_{\lambda\nu}^{\kappa\mu} \\ \langle WU \rangle_{\lambda\nu}^{\kappa\mu} & \langle WW \rangle_{\lambda\nu}^{\kappa\mu} \end{array} \right) \left(\begin{array}{c} u_{\lambda\nu} \\ w_{\lambda\nu} \end{array} \right), \tag{2.19}$$

which clearly involves a very dramatic reduction of $\mathbf{A}_{\lambda\nu}^{\kappa\mu}(t)$. It will be noted that (2.19) is now identical to the equation obtained previously for the unstratified system by Smyth & Peltier (1994).

Owing to the finite memory of available computers, we have of course been obliged to truncate the above Galerkin series representations of the fields and for this purpose have adopted the scheme employed by Klaassen & Peltier (1985b), namely the triangular scheme $2 \mid \lambda \mid + \nu \leqslant N_t$, where N_t is a global truncation level.

Equation (2.18) may be rewritten in the equivalent vector form

$$\frac{\mathrm{d}\boldsymbol{v}}{\mathrm{d}t} = \mathbf{A}(t)\boldsymbol{v}; \qquad \boldsymbol{v} = \left(\begin{array}{c} u_{\lambda\nu} \\ w_{\lambda\nu} \\ \rho_{\lambda\nu} \end{array} \right). \tag{2.20}$$

Depending upon the time-dependence of the basic-state two-dimensional flow, the solution of the evolution equation (2.20) could prove to be very complicated. In the present context, however, our focus will be upon the stability characteristics of two-dimensional vortical basic states which evolve on a timescale that is slow compared to the timescale of the three-dimensional instabilities to which they are subject. In such circumstances we may safely assume that temporal growth of the solution is exponential as $\boldsymbol{v} = \boldsymbol{v}_n \mathrm{e}^{\sigma_n t}$, and (2.20) then reduces to the standard matrix eigenvalue problem:

$$\sigma_n \boldsymbol{v}_n = \bar{\mathbf{A}} \boldsymbol{v}_n; \qquad \bar{\mathbf{A}} = \frac{1}{\tau} \int_{t_1}^{t_2} \mathbf{A}(t') \mathrm{d}t', \tag{2.21}$$

in which σ_n, the eigenvalue of $\bar{\mathbf{A}}$, is an exponential growth rate, $\boldsymbol{v}_n$ is the eigenvector corresponding to this eigenvalue, $\bar{\mathbf{A}}$ is a time-averaged stability matrix corresponding to some time interval $t_1 \leqslant t \leqslant t_2$ with $\tau = t_2 - t_1$ the time interval over which $\mathbf{A}$ exhibits no significant secular variation. If the growth rate of a particular mode of interest is sufficiently large in comparison to some appropriate measure of the rate of evolution of the background two-dimensional flow, then this approach is entirely appropriate. In the analyses to follow, this approach will be justified *a posteriori*. We may take as an appropriate measure of the fluctuations in the two-dimensional Kelvin–Helmholtz flow a 'growth rate' based upon the Kelvin–Helmholtz wave kinetic energy K' (Klaassen & Peltier 1985b), namely

$$\sigma_{2D} = \frac{1}{2K'} \frac{\mathrm{d}K'}{\mathrm{d}t}. \tag{2.22}$$

Thus an eigenvalue and its corresponding eigenvector are a valid representation of one of the realizably unstable modes of the Kelvin–Helmholtz flow only if

$$\sigma_n \gg \sigma_{2D}. \tag{2.23}$$

We employ this separation-of-timescales argument here rather than the TASM method described in Smyth & Peltier (1994) because the latter method is flawed for reasons made clear in Baym (1968).

In what follows we will use the vorticity distribution in the last phase (post-pairing phase) of figure 3 as the first model of the cross-section of a barotropic columnar vortex to be employed as basic state in our analyses of instability. The evolution of
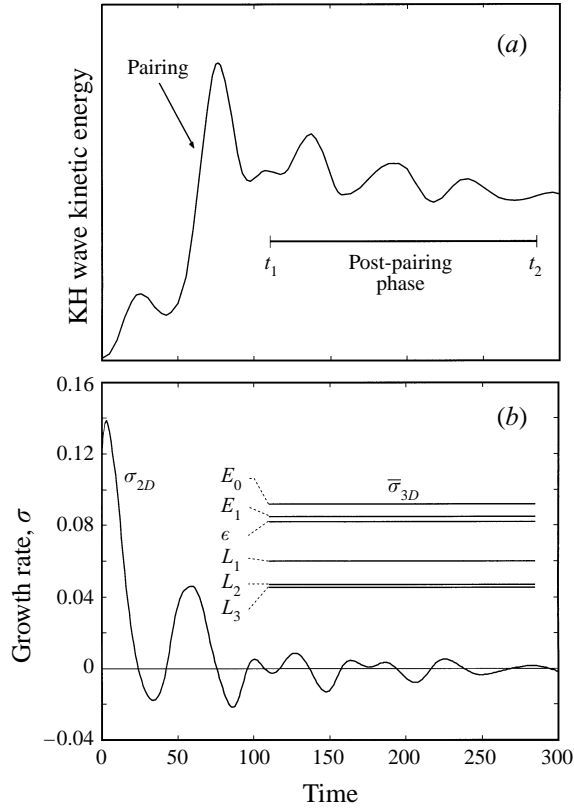
FIGURE 5. The evolution of (*a*) the Kelvin–Helmholtz wave kinetic energy, K', and (*b*) the instantaneous growth rate of the two-dimensional Kelvin–Helmholtz wave, σ_{2D}, with time. The post-pairing phase of the flow corresponds to the time interval marked on the figure ($t_1 = 110$, $t_2 = 285$). $\bar{\sigma}_{3D}$ presents the maximum time-averaged growth rates for the most unstable three-dimensional longitudinal (L_1, L_2, L_3), edge (E_0, E_1) and elliptical (ϵ) modes.

the Kelvin–Helmholtz wave kinetic energy during the post-pairing ($t_1 = 110, t_2 = 285$) phase is quasi-periodic and characterized by a slow viscous diffusion and weak nutation of the vortex core due to the influence of the neighbouring vortices (see figure 5*a*). The evolution of the mean flow is almost time-independent (its energy slowly decreases owing to viscous friction), while the evolution of the Kelvin–Helmholtz wave-related kinetic energy is characterized by a small-amplitude and weakly damped limit-cycle oscillation. Note also that the kinetic energy of the parallel, time-mean component of the flow is much larger than the kinetic energy of the Kelvin–Helmholtz wave. (Detailed discussion of the energy budget for two-dimensional Kelvin–Helmholtz waves will be found in Klaassen & Peltier 1985*a*.) In figure 5(*b*) we have recorded the instantaneous growth rate of the two-dimensional Kelvin–Helmholtz wave, σ_{2D}, as a function of time, together with the time-averaged growth rates of the most unstable three-dimensional modes, $\bar{\sigma}_{3D}$, to be discussed below. The growth rates for all three-dimensional unstable modes are far above the instantaneous growth rate for the Kelvin–Helmholtz wave and this fact clearly justifies our two-timescale approach to the stability analyses of the post-pairing phase of the Kelvin–Helmholtz flow.
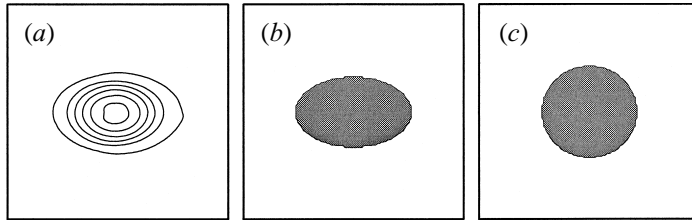
FIGURE 6. The two-dimensional background vorticity fields used as the basic state for the three-dimensional stability analyses: (*a*) the vorticity field averaged on the time interval $110 \leqslant t \leqslant 280$ for the post-pairing phase of the Kelvin–Helmholtz flow; (*b*) the vorticity field for the Kida-like model vortex; (*c*) the vorticity field for the circular limit of the Kida-like model vortex. The visual non-dimensional size of the domain is 28×28.

For future reference, it should also be noted that the stability matrix $\boldsymbol{A}(t)$ is a linear function of the background velocity fields. The time-averaged matrix is therefore equivalent to averaging of the background fields over the time interval $[t_1, t_2]$ and then computing the stability matrix $\bar{\boldsymbol{A}}$ by substituting the time-averaged fields into the defining equations for $\langle UU \rangle_{\lambda v}^{\kappa \mu}$, $\langle UV \rangle_{\lambda v}^{\kappa \mu}$, etc., instead of time-averaging the stability matrix $\boldsymbol{A}(t)$ on the time interval $[t_1, t_2]$. Note that the vector $\boldsymbol{v}$ does not include terms $v_{\lambda v}$ (see (2.20)), so that in order to obtain the y-component of the perturbation velocity we must employ the relevant diagnostic equation (2.16).

3. Columnar vortex stability: the Kelvin–Helmholtz model

In this section we will discuss the stability of the two-dimensional free shear layer, with embedded coherent structure consisting of smooth elliptical vortices, to three-dimensional perturbations. We will initially focus attention upon the barotropic flow that was produced by a single step of the pairing interaction and which was described in §2. On the basis of their stability analyses of the equivalent non-stratified problem, Smyth & Peltier (1994) demonstrated that the instability spectra for three-dimensional perturbations of the Kelvin–Helmholtz flow are self-similar with respect to the phase of the pairing interaction, and this clearly allows us to focus our attention on a single post-pairing phase of the flow. Because the length of the computational domain for the post-pairing phase of the two-dimensional flow equals the wavelength of the train of Kelvin–Helmholtz coherent structures, the secondary instability analyses deliver only unstable modes whose streamwise wavelength is double that of the primary wave (note that for the pre-pairing phase the computational domain contains two wavelengths of the primary Kelvin–Helmholtz instability). We will refer to the unstable modes of this system as longitudinal modes and will denote them by $(L_n, n = 1, 2, 3...)$ following Smyth & Peltier (1994). For the purpose of the stability analyses to be reported here, we employ the standard approach described above with the vorticity field for the post-pairing phase of the two-dimensional Kelvin–Helmholtz flow averaged on the time interval $110 \leqslant t \leqslant 280$. This temporally averaged background vorticity field is shown in figure 6(*a*). The global truncation level for our analyses is set to $N_t = 37$ (significantly higher than it proved possible to achieve in the work of Smyth & Peltier 1994) for all analyses of unstratified flows and to the slightly lower value $N_t = 31$ for all analyses of stratified flows.
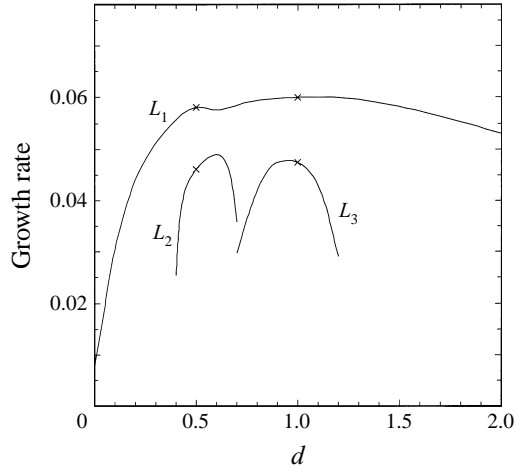
FIGURE 7. The instability spectrum for the non-rotating unstratified Kelvin–Helmholtz wavetrain as a function of spanwise wavenumber d. The plot shows only the most unstable stationary modes; $\times$ denotes modes whose spatial structure are to be displayed in figures 8, 10.

3.1. *The non-rotating problem*

We begin presentation of the results of the stability analyses with those for the special case $f = 0$ ($Ro^{-1} = 0$) and $Fr^{-2} = 0$, which corresponds to the non-rotating and unstratified problem. Results for this special case have been discussed in detail by Smyth & Peltier (1994), and we will only provide a brief overview here in order to fix ideas and to connect the new results that we will obtain to this previous work.

In figure 7, we plot the growth rates, σ, of the most unstable modes for the post-pairing phase of the Kelvin–Helmholtz flow as a function of the spanwise wavenumber d. This spectrum is determined by the eigenvalues of the stability matrix, and in it all modes are stationary (i.e. their growth rates are purely real). The entire set of modes with growth rates higher than $\sigma = 0.043$ is displayed on this figure.

The curve labelled L_1 on figure 7 represents the dominant branch of longitudinal modes in the spectrum and is the counterpart in the present analysis of the structure first identified by Klaassen & Peltier (1991). It will also be noted that the L_1 branch exhibits a sharp 'kink' in the vicinity of $d = 0.6$. Inspection of the spatial structure of the modes along this branch reveals that it changes abruptly at this point from core-centred at low d to braid-centred at high d. The spatial structure of the mode at the point $d = 0.5$ is displayed in figure 8(*a*) in terms of its spatial distribution of perturbation kinetic energy K', spanwise velocity v' and spanwise vorticity ω' in the (X, Z)-plane. The perturbation kinetic energy is quadratic in the disturbance fields, and the figure displays the average of this quantity over a single spanwise wavelength in the form of a positive real function of x and z. The spanwise velocity and vorticity perturbations vary sinusoidally with y, and the corresponding parts of the figure for these eigenfunctions show the corresponding fields evaluated on a plane of constant y, which has been chosen to coincide roughly with the maximum of the perturbation quantity. The modal structure displayed in figure 8(*a*) is core-centred, i.e. the perturbation fields are focused in the vicinity of the core of the two-dimensional elliptical billows.

Considering next the spatial structure of the same L_1 mode but at the point $d = 1.0$ (see figure 8*b*), we note that the kinetic energy perturbation is now concentrated in
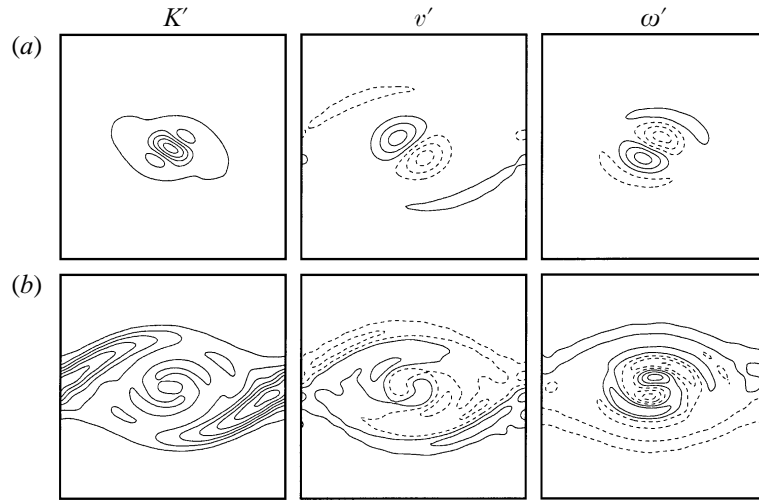
FIGURE 8. The perturbation kinetic energy K', spanwise velocity v' and spanwise vorticity ω' fields in the (X, Z)-plane for the L_1 longitudinal mode at the points: (a) $d = 0.5$ and (b) $d = 1.0$. Solid lines show isolines with positive values while dashed lines represent isolines with negative values. The visual non-dimensional size of the domain is 28×28.

the hyperbolic regions (braids) located between the Kelvin–Helmholtz vortex cores. The absolute maximum growth rate along the L_1 branch of the modal spectrum is found near this value of d but this value of the growth rate for the braid-centred segment of the L_1 branch only slightly exceeds the maximum growth rate for the core-centred segment of this mode. In figures 9(a) and 9(b) we illustrate these two modes along the L_1 branch in the form of isosurfaces of the streamwise component of the perturbation vorticity field.

Since our interest in this paper is primarily in the stability of isolated columnar vortices it should be clear that only the core-centred modes of the L_1 branch would exist on an isolated vortex tube since in that circumstance the 'braid' region does not exist.

The other two branches of longitudinal modes labelled L_2 and L_3 in figure 7 exhibit only slightly lower maximum growth rates in comparison with the L_1 longitudinal mode. The modes along these branches are all core-centred, and spatial structures for them, shown in figure 10, are similar to the structure of the core-centred segment of the L_1 branch. It is clear that all of these core-centred modes correspond to the so-called 'translative' or elliptical instability (Pierrehumbert & Widnall 1982; Bayly 1986; Waleffe 1990; Klaassen & Peltier 1985, 1989, 1991) in that the perturbation vorticity field ω' describes a translation of each vortex in the Kelvin–Helmholtz train in the same direction. Under the assumption that nonlinearity does not alter the fundamental character of the instability, we may infer the way in which the originally columnar vortex would be altered by the growth of the linearly unstable mode. Because the vorticity perturbation is sinusoidal in the y-direction, the translative instability would initially induce bending of the vortex tubes in a sinusoidal fashion with the wavelength corresponding to the most unstable wavelength in the spectrum (Pierrehumbert & Widnall 1982). However, the fastest growing mode in the L_1 branch of the spectrum is not translative and core-centred but rather is braid-centred. The braid-centred mode, which derives from what we might refer to as hyperbolic instability, is the origin of the streamwise vortex streaks whose appearance is precursory to the turbulent
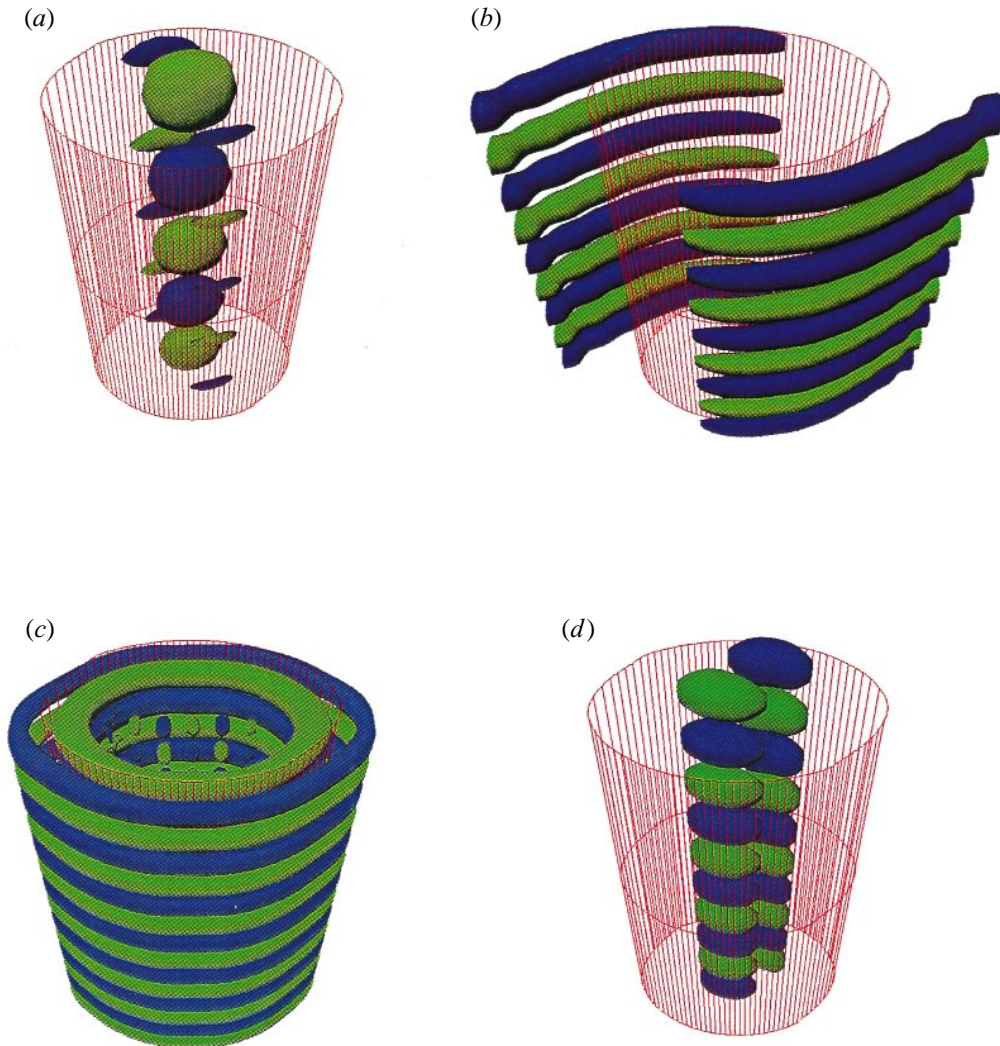
(a)

(b)

(c)

(d)

FIGURE 9. Isosurfaces of the streamwise component of the perturbation vorticity field for (a) the core-centred L_1 mode, (b) the braid-centred L_1 mode; and the spanwise component of the perturbation vorticity field for (c) the edge mode E_0 and (d) the elliptical mode labelled ϵ in the text.

collapse of the unstratified mixing layer (Klaassen & Peltier 1985*b*, 1991; Smyth & Peltier 1991, 1994; Caulfield & Peltier 1994).

We consider next the influence of stratification on the stability characteristics of the post-pairing phase of the elliptical billows. In this case, the gradient of the background density stratification is in the positive *y*-direction and thus is orthogonal to the plane of the two-dimensional flow (see figure 2). Therefore we should expect that stable stratification would increase the stability of the two-dimensional flow to three-dimensional perturbations because the stable stratification adds additional resistance to vertical motion in the system. In the presence of stable stratification the columnar vortices that characterize the post-pairing phase of the Kelvin–Helmholtz flow should be less unstable to three-dimensional perturbations.
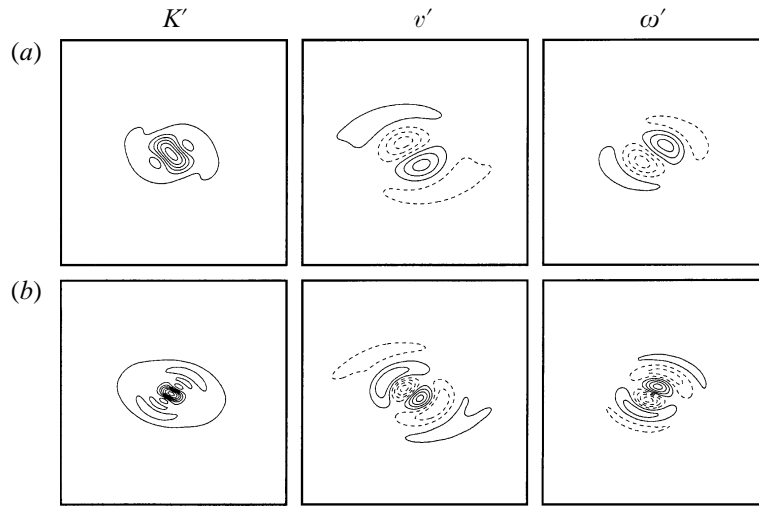
K' v' ω'

(a)

(b)

FIGURE 10. The perturbation kinetic energy K', spanwise velocity v' and spanwise vorticity ω' fields in the (X, Z)-plane: (a) for the L_2 longitudinal mode at the point $d = 0.5$ and (b) for the L_3 longitudinal mode at the point $d = 1.0$. Solid lines show isolines with positive values while dashed lines represent isolines with negative values. The visual non-dimensional size of the domain is 28×28.
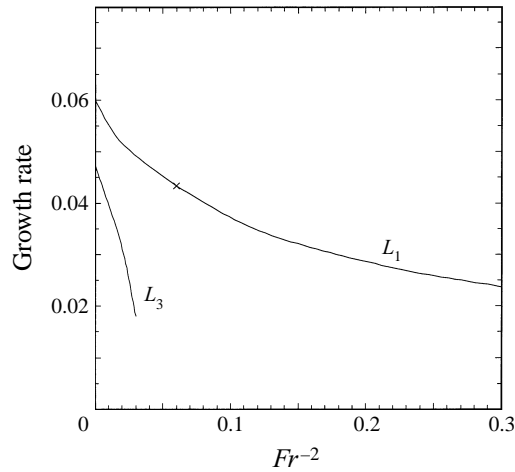
FIGURE 11. The instability spectrum for the non-rotating stratified Kelvin–Helmholtz wavetrain as a function of the inverse square of the Froude number Fr^{-2} at the point $d = 1.0$. The plot shows only the most unstable stationary modes; $\times$ denotes a mode whose spatial structure is to be displayed in figure 12.

On figure 11 we show growth rates of the two most unstable longitudinal modes as a function of the inverse square of the Froude number Fr^{-2} at the point $d = 1.0$. This point corresponds to the maximum growth rate of the dominant braid-centred L_1 longitudinal mode in figure 7 and, therefore, to the most unstable spanwise wavenumber in the non-rotating unstratified problem. As expected, the growth rates of the unstable modes decrease rapidly as the inverse square of the Froude number rises. The L_1 longitudinal mode, which was the most unstable in the non-rotating unstratified case, remains dominant in the spectrum of the non-rotating stratified
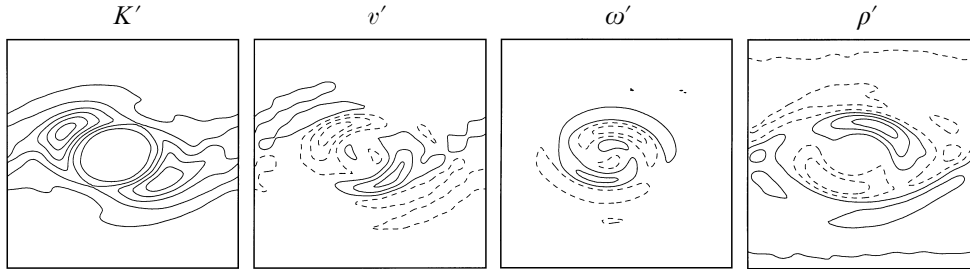
FIGURE 12. The perturbation kinetic energy K', spanwise velocity v', spanwise vorticity ω' and density ρ' fields in the (X, Z)-plane for the L_1 longitudinal mode at the point $Fr^{-2} = 0.06$ ($d = 1.0$). Solid lines show isolines with positive values while dashed lines represent isolines with negative values. The visual non-dimensional size of the domain is 28×28.
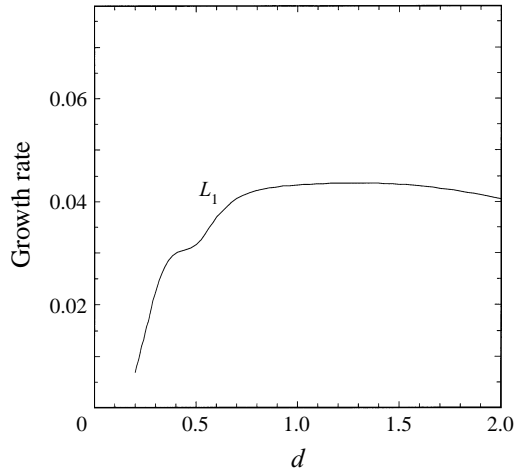

FIGURE 13. The instability spectrum for the non-rotating stratified Kelvin–Helmholtz wavetrain as a function of spanwise wavenumber d at the point $Fr^{-2} = 0.05$. The plot shows only the most unstable stationary modes.

environment. It will be noted that even weak density stratification ($Fr^{-2} = 0.2$) forces the growth rate for this mode to decrease by almost a factor two. The spatial structure of this mode at the point $Fr^{-2} = 0.06$ is presented in figure 12. If we compare this with the spatial structure of the dominant mode in the unstratified case, it will be clear that in general the mode becomes more core-centred as the stratification increases. Maxima of perturbation kinetic energy are now centred closer to the core of the vortex, while for the unstratified case the mode was shown to nucleate in the braids between successive billow cores.

The spectrum in figure 11 demonstrates the influence of stratification on the instability process only at the single fixed value of the spanwise wavenumber $d = 1.0$, and, therefore, on the basis of this restricted analysis we may say nothing concerning the behaviour of the unstable modes at different spanwise wavenumbers. To investigate this aspect of the problem, we have also computed growth rates of the most unstable modes as a function of the spanwise wavenumber d at fixed $Fr^{-2} = 0.05$ and the results are presented in figure 13. If we compare this spectrum to that for the unstratified problem (see figure 7), it will be noted that the only branch of longitudinal modes shown on figure 7 which survives in the presence of stratifi-

cation is the L_1 branch. No other modes with growth rates higher than $\sigma = 0.025$ exist in the spectrum at this value of the Froude number. The L_2 and L_3 unstable longitudinal modes have been entirely stabilized by the stratification and thus disappear from the spectrum. One will also note that the L_1 longitudinal mode holds its position in the spectrum and is not shifted towards higher spanwise wavenumbers by the action of stratification. Another important conclusion implied by the results of these analyses is that the L_1 branch is affected unevenly by stratification. The growth rates for the core-centred part of this longitudinal branch at low spanwise wavenumbers decrease much more rapidly as the inverse square of the Froude number rises than the braid-centred (hyperbolic) part of the same branch at high wavenumbers. This results in strong deformation of the shape of the L_1 growth rate curve by reducing growth rates along the core-centred (elliptical) part of this branch at low spanwise wavenumbers. The other effect of this scale-selective influence of the stratification on the L_1 branch is that the scale at the absolute maximum in growth rate is slightly shifted to higher spanwise wavenumbers from $d = 1.0$ to $d = 1.3$.

3.2. *The rotating case*

Having confirmed the expected stabilizing affect of the density stratification on a columnar vortex, we are in a good position to add the influence of rotation to the mix of physical interactions that collectively control the stability of the two-dimensional column. As previously discussed, we will assume the rotation to be characterized by angular frequency $\Omega = \frac{1}{2}f$, where f is the so-called Coriolis parameter which appears in the context of analyses of geophysical flows where it represents the local vertical component of the angular velocity of the planet. The vector of background rotation is parallel to the y-axis, so that the background vorticity, represented by $\boldsymbol{f}$, is aligned with the relative vorticity field of the two-dimensional flow and with the gradient of the density stratification (see figure 2). Note also that, in the case illustrated, the relative vorticity of the two-dimensional flow is positive while the vector $\boldsymbol{f}$ points in the negative direction along the y-axis.

The Taylor–Proudman theorem (e.g. Greenspan 1968) is often interpreted to suggest that rotating flows should tend to be much more two-dimensional than they would be in the absence of rotation. In the present context this theorem might be interpreted to imply that rotating two-dimensional flows should tend to be more stable to three-dimensional perturbations if the ambient rotation is sufficiently strong (i.e. the Rossby number is sufficiently small). In the circumstances of interest to us here, the two-dimensional flow possesses rather strong relative vorticity $\omega(x, z)$ concentrated within the individual vortex cores. If the value of background rotation f is negative, which corresponds to cyclonic vortices in the present context, three-dimensional motion will be affected by effectively higher rotation $f + \omega(x, z)$ (note again that the vectors $\boldsymbol{f}$ and $\omega(x, z)$ are anti-parallel), and as a result, the rotation may be expected to have a net stabilizing effect. When the value of the background rotation f is positive, which corresponds to anticyclonic vortices, however, and when it is close to the value of the relative vorticity $\omega(x, z)$, then the absolute vorticity $\omega(x, z) - f$ will be close to zero and this circumstance might be expected to lead to higher sensitivity of the two-dimensional flow to three-dimensional perturbations. We might therefore expect that small positive values of background rotation f will tend to make the two-dimensional Kelvin–Helmholtz flow less stable to three-dimensional disturbances. We may also expect that stabilization will be achieved for smaller negative values of background rotation than for positive values.

The stability analysis for the special case of rotating unstratified flow ($Ro^{-1} \neq 0$, $Fr^{-2} = 0$) was discussed in Smyth & Peltier (1994). Here we will briefly review the basic results for this case and then extend them to the much more mathematically challenging stratified circumstance.

The stability analysis for the rotating case may be performed using the same two-dimensional basic state which was employed in the previous subsection (see figures 3 and 6*a*) because rotation has no effect on the two-dimensional flow itself if the influence of rotation is considered from an f-plane perspective. In this subsection we will once more focus our attention entirely on the post-pairing phase of the two-dimensional flow. There is no significant loss of generality because of this, since the instability spectra during different phases of two-dimensional flow evolution are similar to each other and relations among them have been described in detail in Smyth & Peltier (1994). This will also allow us to avoid the unnecessary complications that would otherwise arise in dealing with subharmonic and longitudinal modes simultaneously. Note that during the post-pairing phase there are only longitudinal modes with wavelength equal to the length of the domain because only a single vortex exists in the domain (see figure 3) and the periodic boundary conditions prevent further vortex merging. The time-averaged vorticity field employed for the calculation of the stability matrix $\bar{\mathbf{A}}$ in the post-pairing phase of the two-dimensional flow is once more that presented in figure 6(*a*).

Figure 14 shows the instability spectra for the most unstable modes of the rotating unstratified problem as a function of the inverse Rossby number $Ro^{-1} = f/(U_0/h)$. The spanwise wavenumber for these calculations was set to $d = 1.0$ for the analyses that produced the results shown in figure 14(*a*) and $d = 1.6$ for those shown in figure 14(*b*). The modal branch with the maximum growth rate at $f = 0$ is composed of a sequence of modes with purely real growth rate. This branch clearly represents the continuation of the L_1 longitudinal branch of braid modes (see figures 7 and 8*b*) to non-zero values of f. As is clear by inspection of figure 14, the maximum growth rate of the L_1 mode corresponds to the point $f = 0$ and this mode is rapidly stabilized for increasing finite $|f|$. In figure 14(*a*), and below the L_1 branch of modes in growth rate, there exists a branch of core-centred modes. The growth rates for this sequence of modes are also purely real and weaker than those along the L_1 branch. The spatial structures of the modes along this branch allows us to identify them as representing the continuation of the L_3 branch of longitudinal modes to non-zero values of f. Like the L_1 mode, the L_3 modes have their maximum growth rates at the point $f = 0$ and growth rate decreases for increasing $|f|$ although the rate of stabilization by the background rotation is somewhat reduced from that which characterizes the L_1 sequence. This mode does not exist for $d = 1.6$ (see figure 7) and, therefore, it is not shown in figure 14(*b*).

The most intense instabilities that arise in the rotating problem, however, are those that lie along the branch on which growth rate peaks in the vicinity of $Ro^{-1} = 0.2$, in which case the vorticity in the basic state has opposite sign to the background rotation. Once more the modes along this branch have purely real growth rates. Figure 15(*a*) displays the spatial structure of this dominant mode. Its perturbation kinetic energy is seen to be concentrated in a ring around the two-dimensional vortex core, so that, following Smyth & Peltier (1994), this mode will be referred to as the fundamental edge mode E_0. This mode represents an entirely new class of modes which has no counterpart in the non-rotating problem. The mode achieves its maximum growth rate $\sigma = 0.092$ in the vicinity of the point $Ro^{-1} = 0.2$, $d = 1.6$ (see figure 14*b*) which may be compared to the much lower growth rate $\sigma = 0.06$
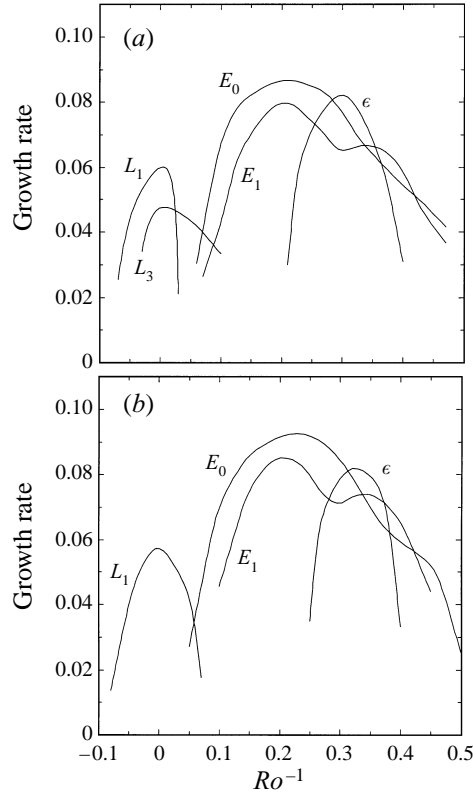
FIGURE 14. The instability spectrum for the rotating unstratified Kelvin–Helmholtz wavetrain as a function of inverse Rossby number $Ro^{-1} = f(U_0/h)^{-1}$ at the point (a) $d = 1.0$, (b) $d = 1.6$. The plot shows only the most unstable modes.

for the fastest growing mode along the L_1 branch in the non-rotating problem. This new mode is therefore expected to play a crucial role in the evolution of anticyclonic vortices for slow background rotation. The growth rate of the edge mode rapidly decreases for $Ro^{-1} \leqslant 0.07$ and $Ro^{-1} \geqslant 0.5$. As expected on the basis of the previous comments related to the Taylor–Proudman theorem, we find that fast background rotation for vortices of either sign strongly stabilizes the two-dimensional coherent vortical structures to three-dimensional perturbations, while slow rotation, when the vector $\boldsymbol{f}$ is antiparallel to the vector of relative vorticity $\omega(x, z)$, which corresponds to anticyclonic vortices in our case, acts to destabilize the flow.

The E_1 branch of modes that also appears on figure 14 corresponds to the first harmonic of the edge mode sequence. This mode is weaker than the fundamental and stationary edge mode E_0 but it exhibits sufficiently large growth rate that it could exert substantial influence on the evolution of the coherent structure, depending on the initial conditions. Note that the growth rate of the first subharmonic edge mode E_1 is actually higher than the growth rate of the stationary edge mode E_0 near $Ro^{-1} = 0.37$. The spatial structure of this mode is similar to the structure of the stationary edge mode and is not shown here.

The final branch of modes shown on figure 14 (labelled ϵ) represents a highly core-centred mode with purely real growth rate. This mode achieves its maximum growth near the point $Ro^{-1} = 0.3$ and its growth rate exceeds the growth rate of the
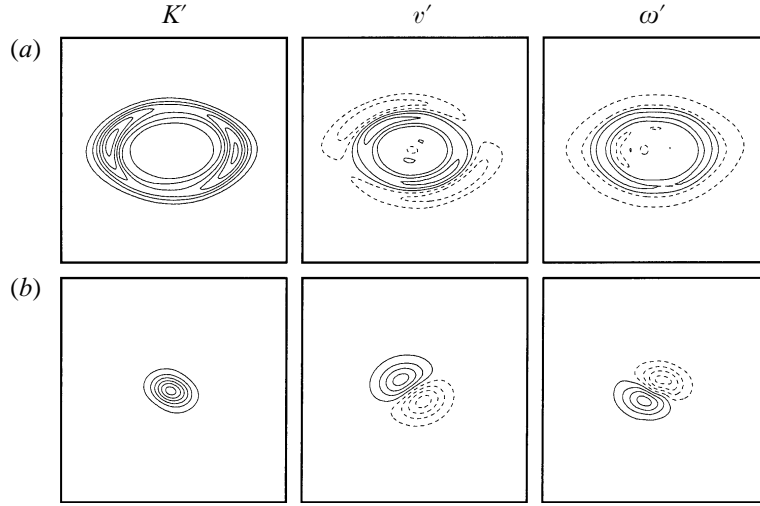
FIGURE 15. The perturbation kinetic energy K', spanwise velocity v' and spanwise vorticity ω' fields in the (X, Z)-plane: (a) for the E_0 edge mode at the point $Ro^{-1} = 0.21$ ($d = 1.0$) and (b) for the ϵ elliptical mode at the point $Ro^{-1} = 0.30$ ($d = 1.0$). Solid lines show isolines with positive values while dashed lines represent isolines with negative values. The visual non-dimensional size of the domain is 28×28.

dominant E_0 edge mode at this point. The spatial structure of the mode is shown in figure 15(b). It is indeed highly core-centred and its structure is similar in form to that of the core-centred longitudinal modes in the non-rotating case, but we could find no counterpart of this mode in the non-rotating problem. This branch has been identified as a mode related to the elliptical instability because it exists only for elliptical vortices (see the discussion of the results for the circular limit of the 'Kida-like' vortex below). In the previous unstratified rotating analyses of Smyth & Peltier (1994) the ϵ mode was overlooked owing to the relatively low resolution at which it was possible to solve the eigenproblem. In parts (c) and (d) of the previously discussed figure 9 are shown isosurfaces of the vertical perturbation vorticity field for both the edge and ϵ modes.

It was pointed out in Smyth & Peltier (1994) that the physical mechanism of instability for the edge mode is most usefully understood in terms of the inertial (centrifugal) mechanism. Rayleigh's standard criterion (e.g. Chandrasekhar 1968) for this mechanism asserts that in the absence of viscous effects the necessary and sufficient condition for a distribution of azimuthal velocity $V(r)$ (where r is the radius) of an axisymmetric flow to be stable is simply

$$\frac{\mathrm{d}}{\mathrm{d}r}(Vr)^2 > 0 \tag{3.1}$$

everywhere in the interval, and, further, that the distribution is unstable if $(Vr)^2$ should decrease anywhere within the interval. This criterion may be simply derived using energy arguments and the same arguments may be applied in a rotating reference frame, provided that the azimuthal velocity and vorticity are evaluated in the inertial frame. The simple modification of the usual Rayleigh criterion for stability which follows from such analysis (Kloosterziel & van Heijst 1991) is just

$$\frac{\mathrm{d}}{\mathrm{d}r}(Vr - \tfrac{1}{2}fr^2)^2 > 0. \tag{3.2}$$

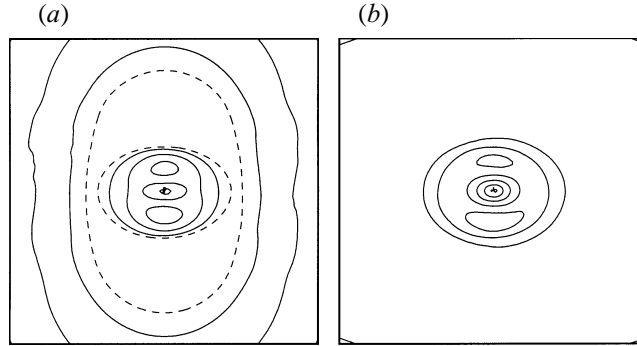(*a*)   (*b*)

FIGURE 16. The modified Rayleigh's criterion for the post-pairing phase of the Kelvin–Helmholtz shear flow (*a*) for slow negative background rotation (anticyclonic vortex) $Ro^{-1} = 0.2$, (*b*) for slow positive background rotation (cyclonic vortex) $Ro^{-1} = -0.2$. Dashed lines reveal the region where the modified Rayleigh's criterion is violated $(Ro\tilde{V} - \frac{1}{2}\tilde{r})(Ro\tilde{\omega} - 1) < 0$.

Note that the original criterion is recovered in the limit $f \to 0$. In terms of non-dimensional variables we may re-write this extended Rayleigh criterion in the form

$$(Ro\,\tilde{V} - \tfrac{1}{2}\tilde{r})(Ro\,\tilde{\omega} - 1) > 0 \tag{3.3}$$

in which Ro is the Rossby number, $\tilde{V}$ is the non-dimensional azimuthal velocity, $\tilde{\omega}$ is the non-dimensional vorticity and $\tilde{r}$ is the non-dimensional radius.

In the case of the specific columnar vortex of interest to us here, the spatial location of the edge mode corresponds quite closely to the region in which the modified Rayleigh criterion is violated for an anticyclonic vortex when the background rotation is relatively slow and, therefore, suggests the possibility of instability (see figure 16*a*). On the other hand, the extended Rayleigh criterion for stability is well satisfied for the same value of background rotation for the cyclonic vortex (see figure 16*b*) and in accord with the results of our analysis the edge mode does not exist in this circumstance.

These arguments allow us to suggest that the instability mechanism for the edge mode is essentially centrifugal, although it is clear in the present context that Rayleigh's assumption of axisymmetric flow is violated. Our fastest growing modes are found to exist for finite d and their growth rates decrease towards zero in the limit $d \to 0$. There is an obvious analogy that may usefully be drawn with the problem of cylindrical Couette flow.

In figure 17, we plot growth rates of the most unstable edge modes as a function of the inverse square of the Froude number Fr^{-2} at the point $Ro^{-1} = 0.21$, $d = 1.0$. This value of the Rossby number corresponds to the point of greatest instability of the spectrum shown in figure 14(*a*). It will be observed by inspection of the results displayed on the figure that the general behaviour of the most unstable edge modes in the rotating case, with increasing density stratification, is similar to the behaviour of the most unstable longitudinal modes in the non-rotating case. As expected, the growth rates of the unstable modes decrease rapidly as the inverse square of the Froude number rises. The growth rate of the dominant mode in the unstratified case (on the E_0 branch) decreases dramatically in the presence of stratification at this wavenumber, and by $Fr^{-2} = 0.03$ its growth rate is essentially negligible. At this value of d, the E_1 edge mode then becomes the dominant source of instability in the spectrum as the stratification increases because it is stabilized much more slowly
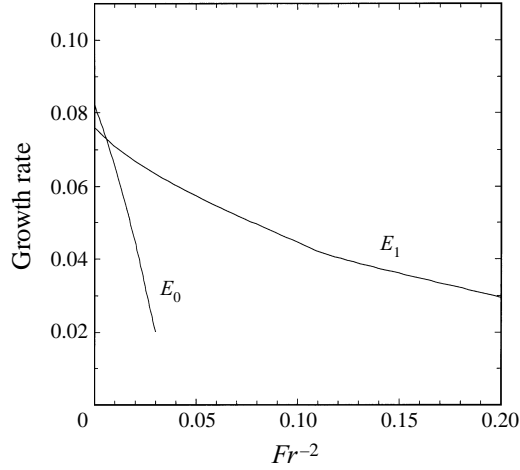
FIGURE 17. The instability spectrum for the rotating stratified Kelvin–Helmholtz wavetrain as a function of the inverse square of the Froude number Fr^{-2} at the point $d = 1.0$, $Ro^{-1} = 0.21$. The plot shows only the most unstable modes.

than is the E_0 mode. In general, however, the edge modes remain dominant in the spectrum for this Rossby number and we do not observe the appearance of any additional modes of instability.

In figure 18, we show the growth rate spectrum for the most unstable modes of the rotating stratified problem as a function of the inverse Rossby number $Ro^{-1} = f/(U_0/h)$ at fixed $Fr^{-2} = 0.05$. The spanwise wavenumber was taken to be $d = 1.0$ in figure 18(a) and $d = 2.5$ in figure 18(b). Comparing these results with the modal spectra shown on figure 14, we may conclude that, similarly to the non-rotating problem (see figures 7 and 13), stable stratification affects different modes of instability unevenly. The fundamental and the most unstable mode for the rotating unstratified problem, the E_0 edge mode, is stabilized most rapidly and disappears from the spectrum by $Fr^{-2} = 0.05$ at $d = 1.0$. At the same time this mode continues to exist at the higher spanwise wavenumber $d = 2.5$ and maximum growth occurs at the same value of Ro^{-1}. It can then be concluded that the scale-selective action of stable stratification on the unstable modes shifts the scale of maximum growth of the E_0 edge mode to slightly higher wavenumbers compared with the unstratified case. The first harmonic of the fundamental branch of edge modes, E_1, is affected less strongly by the stratification and still exists in the instability spectra for both values of d. Maximum growth rate continues to occur at the same value of Ro^{-1}, although the form of the E_1 curve is slightly deformed. The L_1 longitudinal branch also remains in the spectrum and continues to exhibit maximum growth at zero background rotation. The elliptical mode labelled ϵ is the mode which is least affected by stable stratification, and its growth rate is far in excess of the edge branch of modes. As stated previously, the elliptical mode has not been identified in any previous analysis of this kind.

On the basis of the analyses presented in this section we may conclude that stable stratification stabilizes the barotropic vortex column generated by the pairing interaction in the shear layer. This is the case both in the presence and in the absence of rotation, although the influence of stable stratification is strongly scale selective. We do not observe the appearance of new unstable modes in the stratified case, and
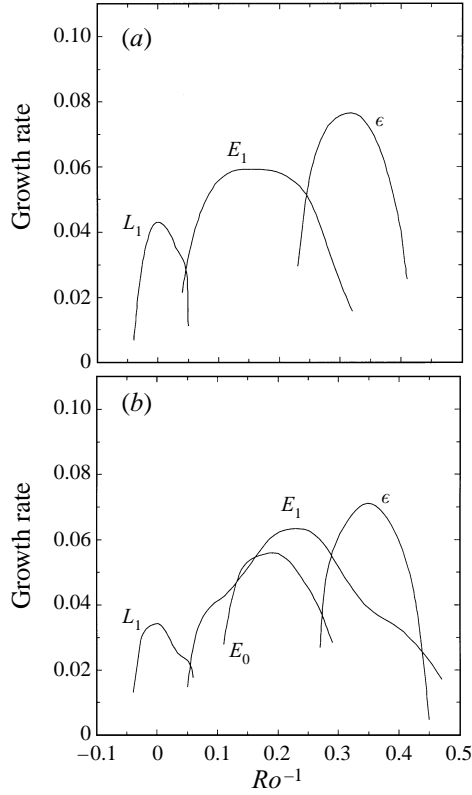
FIGURE 18. The instability spectrum for the rotating stratified Kelvin–Helmholtz wavetrain as a function of inverse Rossby number $Ro^{-1} = f(U_0/h)^{-1}$ at the point $Fr^{-2} = 0.05$ and (a) $d = 1.0$, (b) $d = 2.5$. The plot shows only the most unstable modes.

we may therefore conclude that the mechanisms of instability remain the same in the presence of stable stratification. The only effect introduced by the density stratification is the rapid stabilization of all unstable modes as the inverse square of the Froude number rises. As mentioned above, this result was not unexpected.

4. Columnar vortex stability: the Kida-like model

In the previous section we discussed the results obtained on the basis of three-dimensional instability analyses of the vortex column formed by the merger of two Kelvin–Helmholtz vortices. In the next step of analysis, we wish to examine the influence of the precise form of the background vorticity distribution inside the vortex core on the dominant modes of three-dimensional instability of a vortex column under the action of background rotation and stratification. In order to study this aspect of the problem, we will employ the second model (the Kida-like model) described above as the vorticity distribution in the two-dimensional basic state for the purpose of the three-dimensional stability analyses. Our intention is to compare the stability properties of the Kida-like model to three-dimensional perturbations with the stability properties previously derived using the much more complex quasi-elliptical and quasi-Gaussian continuous vorticity distribution produced as numerical end product of a single pairing interaction between two Kelvin–Helmholtz billows.
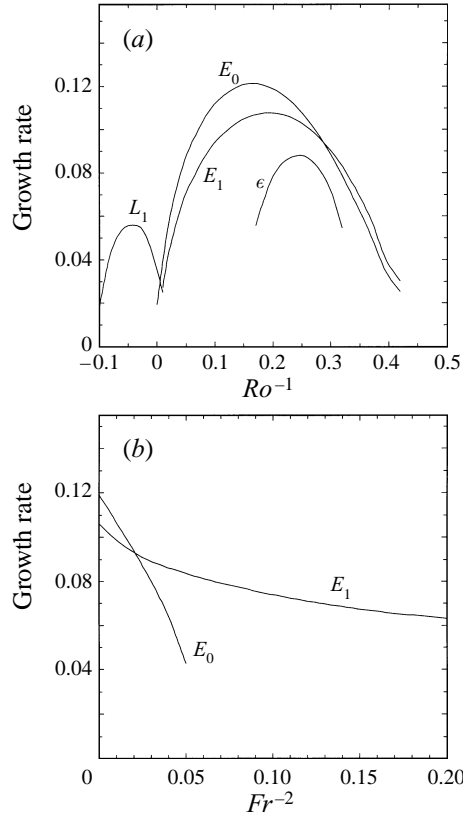
FIGURE 19. The instability spectra for (a) the rotating unstratified Kida-like model vortex as a function of inverse Rossby number $Ro^{-1} = f(U_0/h)^{-1}$ at the point $d = 1.0$ and (b) the rotating stratified Kida-like model vortex as a function of the inverse square of the Froude number Fr^{-2} at the point $d = 1.0$, $Ro^{-1} = 0.17$. The plot shows only the most unstable modes.

4.1. The Kida-like vortex with ellipticity matched to the Kelvin–Helmholtz case

We begin by directing attention to the Kida-like vortex with the ellipticity set equal to that of the time-averaged vorticity field that arose in the post-pairing phase of the evolving free shear layer and will first focus our attention on an investigation of the rotating unstratified problem ($Ro^{-1} \neq 0$, $Fr^{-2} = 0$). Figure 19(a) presents growth rates for the most unstable modes as a function of inverse Rossby number (Ro^{-1}) with the spanwise wavenumber fixed to the value $d = 1.0$. If one compares this instability spectrum with that for the rotating unstratified analysis of the Kelvin–Helmholtz billow (see figure 14), it is very clear that a high degree of similarity exists. The dominant mode in the spectrum for the anticyclonic vortex, when the background rotation is relatively slow, once more has purely real growth rate. The eigenfunctions that determine the spatial localization of this mode are again concentrated in a ring surrounding the core of the background vortex and the spatial structure of the mode (not shown here) is therefore similar to the E_0 edge mode for the Kelvin–Helmholtz basic state (see figure 15a). The E_0 mode for the Kida-like model achieves its maximum growth rate at slightly higher Rossby number corresponding to $Ro^{-1} = 0.17$ compared to $Ro^{-1} = 0.21$ for the Kelvin–Helmholtz basic state. The growth rate of this mode also rapidly decreases for $Ro^{-1} < 0.05$ and $Ro^{-1} > 0.35$. The E_1 branch again corresponds

to the first harmonic of the edge mode sequence. It is slightly weaker than the fundamental mode in the case of the Kelvin–Helmholtz shear flow and has similar spatial structure. This mode becomes dominant in the region $Ro^{-1} > 0.3$, again similar to the result obtained for the Kelvin–Helmholtz case. The branch of modes with maximum growth rate for small Ro^{-1} may be identified as the L_1 longitudinal mode and clearly corresponds to the L_1 mode for the Kelvin–Helmholtz vortex. In the present case of the Kida-like vortex, however, the L_1 longitudinal mode exhibits maximum growth rate at $Ro^{-1} = -0.04$, while in the case of the Kelvin–Helmholtz background flow the L_1 mode has maximum growth rate for precisely zero background rotation. The last modal curve, labelled ϵ, exhibits highly core-centred spatial structure and is similar to the elliptical mode that was shown to exist in the case of the Kelvin–Helmholtz billow. In the present case, however, the mode exhibits maximum growth rate at the slightly lower value of background rotation $Ro^{-1} = 0.25$ in comparison with $Ro^{-1} = 0.30$ for the Kelvin–Helmholtz basic state. It will also be noted that the growth rate of this mode does not exceed the growth rate of the edge branch of modes for any value of the background rotation at the spanwise wavenumber $d = 1.0$.

To continue our analysis of the stability of the Kida-like vortex, we investigate the influence of stratification on the rotating problem at the point which corresponds to the most unstable Rossby number. Figure 19(*b*) presents growth rates for the most unstable modes as a function of the inverse square of the Froude number for the rotating stratified Kida-like model vortex at $Ro^{-1} = 0.17$. Again, inspection of the resulting spectrum for the Kida-like model reveals great similarity in its general form to the spectrum for the Kelvin–Helmholtz vortex (see figure 17). The E_0 edge mode is rapidly quenched as the inverse square of the Froude number increases, and the growth rate of the mode is reduced by more than a factor two by $Fr^{-2} = 0.05$. The behaviour of this mode is therefore very similar to the behaviour of the E_0 mode in the spectrum of the Kelvin–Helmholtz vortex, but the E_0 edge mode is stabilized about twice as rapidly by increasing stratification as is the case in the spectrum of the Kelvin–Helmholtz flow. Again, the E_1 mode is stabilized much more slowly than the E_0 mode at this wavenumber and becomes dominant in the spectrum for sufficiently large Fr^{-2}.

Thus, the general behaviour of the unstable modes and thus the instability mechanisms for the rotating stratified and rotating unstratified cases of the elliptical Kida-like model vortex are very similar to those for the Kelvin–Helmholtz vortex. We have therefore demonstrated that the details of the vorticity distribution in elliptical vortices do not significantly influence the instability of the coherent columnar vortical structure to three-dimensional perturbations.

4.2. *The circular limit of the Kida-like model*

A further issue that clearly arises from these analyses concerns the influence of the ellipticity of the background vortex itself on three-dimensional instability. It might be expected that the ellipticity should not significantly influence the instability mechanism for rotating and stratified cases, at least for modes which are not themselves essentially elliptical (translative) in their nature. To investigate the validity of this assumption we have also performed similar instability analyses using the circular limit of the Kida-like model vortex as the two-dimensional background vorticity distribution for the linear three-dimensional stability analysis.

We begin once more with an investigation of the rotating unstratified problem ($Ro^{-1} \neq 0$, $Fr^{-2} = 0$). The instability spectrum for this case for the spanwise wavenumber $d = 1.0$ is shown in figure 20(*a*). Only the most unstable modes are pre-
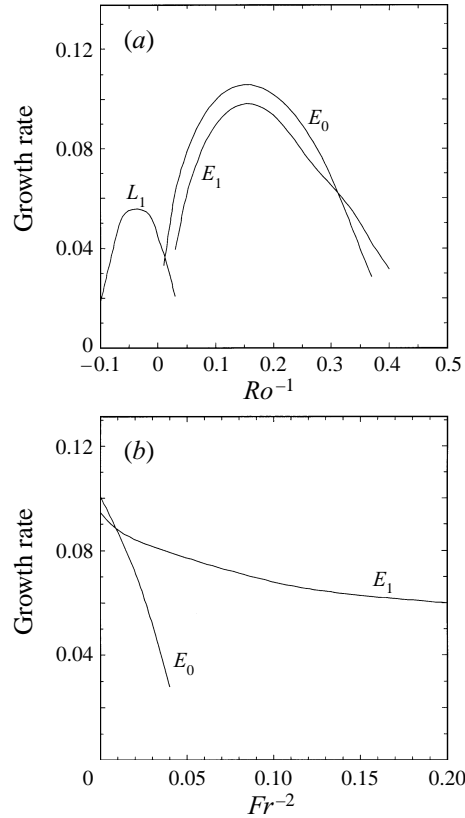
FIGURE 20. The instability spectra for (*a*) the rotating unstratified circular vortex as a function inverse Rossby number $Ro^{-1} = f(U_0/h)^{-1}$ at the point $d = 1.0$ and (*b*) the rotating stratified circular vortex as a function of the inverse square of the Froude number Fr^{-2} at the point $d = 1.0$, $Ro^{-1} = 0.15$. The plot shows only the most unstable modes.

sented. As expected, the general form of the spectrum is similar to the corresponding spectrum for the elliptical Kida-like vortex (see figure 19*a*) and the Kelvin–Helmholtz vortex (see figure 14) cases. The fundamental harmonic E_0 of the edge mode family is again the dominant mode of instability for anticyclonic vortices when the background rotation is relatively slow. The mode reaches its maximum growth rate at the point $Ro^{-1} = 0.15$, which is close to the value at which the elliptical Kida-like vortex was found to be most unstable ($Ro^{-1} = 0.17$). The first harmonic E_1 of the edge mode sequence is in general slightly weaker than the E_0 mode but again becomes dominant in the region $Ro^{-1} > 0.3$. Its spatial structure is similar to that of the dominant E_0 mode. The growth rates of all edge modes decrease rapidly to zero in the region $Ro^{-1} < 0.15$ and $Ro^{-1} > 0.30$. In the region of high Rossby numbers corresponding to slow or vanishing background rotation the L_1 longitudinal mode is again dominant. It achieves maximum growth rate at the point $Ro^{-1} = -0.04$ but remains dominant in the non-rotating case ($Ro^{-1} = 0$). The main difference in the spectrum for the circular Kida-like vortex from those for the Kelvin–Helmholtz elliptical billow and the elliptical Kida-like vortex is that the elliptical ϵ mode no longer exists. This fact rather clearly justifies the identification of this unstable mode as an elliptical instability. The existence of this elliptical mode is determined not only by the ellipticity of the vortex but also by the background rotation. Similarly to the edge mode, this elliptical

mode exists in instability spectra only for anticyclonic vortices when the background rotation is relatively slow.

Figure 20(*b*) presents the spectrum for the rotating stratified case of the circular vortex at the point $Ro^{-1} = 0.15$, which corresponds to the most unstable Rossby number in the unstratified case for the spanwise wavenumber $d = 1.0$. Only the most unstable modes are shown. Again as expected, the behaviour of the spectrum is very similar to that realized in the case of both the elliptical vortex (see figure 19*b*) and the Kelvin–Helmholtz vortex (see figure 17). The E_0 edge mode, which is dominant in the unstratified case, stabilizes quickly and disappears by $Fr^{-2} = 0.05$. The first harmonic E_1 of the edge mode family stabilizes more slowly than the principal E_0 mode as the inverse square of the Froude number rises and soon becomes dominant.

On the basis of this example, we may conclude, because the instability spectra for the circular and elliptical Kida-like vortices differ only slightly, that the basic ellipticity of coherent vortical structures in strain does not significantly influence their dominant mechanisms of instability, except over the limited range of background rotation in the vicinity of $Ro^{-1} = 0.3$ where the elliptical mechanism of instability exists only if the columnar vortex itself has an elliptical cross-section.

5. Summary

The goal of the analyses presented herein has been to investigate the linear stability of two-dimensional, columnar, vortical basic states to three-dimensional perturbations in the presence of both background rotation and stable stratification. For the purpose of these analyses, it has been assumed that the stabilizing basic-state density gradient is aligned with the axis of the basic-state vortex tube but that the basic-state rotation may be either positive (in the same sense as the vorticity in the basic state), which corresponds to the cyclonic vortex in our context, or negative (in the opposite sense as to the vorticity in the basic state), which corresponds to the anticyclonic vortex. The influence of rotation on the stability characteristics of the flows has been included in the f-plane approximation. The Boussinesq approximation has been employed in accounting for the influence of density stratification.

The methodology that we have developed for performing such theoretical linear stability analyses is by now well-known. It enables us to reduce the three-dimensional linear perturbation equations that determine the stability of a two-dimensional basic state into the form of a standard matrix eigenvalue problem whose solution reveals the instability characteristics of the two-dimensional background flow. The theoretical methodology previously devised has been extended herein so as to enable us to incorporate the influence of stable density stratification along the axis of the basic-state barotropic vortex.

In the initial stage of the analyses reported herein, we focused on the stability of a train of two-dimensional Kelvin–Helmholtz billows. It had been demonstrated in previous work (Smyth & Peltier 1994) that instability characteristics of the flow for the pre-pairing, pairing and post-pairing phases of the Kelvin–Helmholtz flow in the absence of rotation and stratification were self-similar. This clearly allowed us to direct our attention to a single post-pairing phase in the evolution of the train of vortical structures, and on the basis of our analyses to reconfirm the results obtained in this previous work. It has been found that the spectrum of secondary instability is dominated at low spanwise wavenumbers ($d < 0.6$) by the core-centred segment of the L_1 branch of longitudinal modes in which the perturbation kinetic energy is concentrated in the vortex cores, but for high wavenumbers ($d > 0.6$) by the

segment of the L_1 branch of longitudinal modes in which the perturbation kinetic energy is concentrated in the strained regions between the primary vortices. The most unstable point in the spectrum corresponds to spanwise wavenumbers close to $d = 1.0$, confirming the results of the instability analysis reported previously by Smyth & Peltier (1994) which were conducted at lower resolution.

Our first extension of this previous work to the non-rotating and along-axis-stratified Kelvin–Helmholtz flow ($Ro^{-1} = 0$, $Fr^{-2} \geqslant 0$) revealed that the L_1 branch of longitudinal modes remains dominant in the spectrum but that even weak density stratification ($Fr^{-2} \approx 0.2$) forces the growth rate for this mode to decrease substantially. For sufficiently strong density stratification the three-dimensional instability would appear to be entirely suppressed. No additional modes of instability appear in the spectrum as a consequence of the stratification.

In the next step of our analysis, we recovered the results of previous analyses (Smyth & Peltier 1994) for the rotating unstratified Kelvin–Helmholtz vortex train. We thereby sought to demonstrate that weak rotation which tends to bring the absolute vorticity of the two-dimensional anticyclonic flow closer to zero acts to destabilize the flow. Maximum destabilization was found at the vicinity of the point $Ro^{-1} = 0.2$, $d = 1.6$. The perturbation kinetic energy of the most unstable mode was shown to be concentrated around the edge of the two-dimensional vortex and, therefore, we continue to refer to this mode, following Smyth & Peltier (1994), as the edge mode. For this wavenumber the maximum growth rate for the E_0 edge mode is $\sigma = 0.092$ for non-zero background rotation in comparison with $\sigma = 0.06$ on the L_1 branch of longitudinal modes for the non-rotating case. Therefore, the edge mode is expected to play a crucial role in the evolution of columnar vortex flow in the presence of background rotation. We have also provided good reason to believe that the mechanism that underlies the edge modes is essentially centrifugal. The spatial location of the edge modes does indeed correspond in an approximate sense to the region in which the modified Rayleigh stability criterion is violated. It is important to note, however, that Rayleigh's assumption of axisymmetric flow may be strongly violated in our case. As expected in consequence of the Taylor–Proudman theorem, however, we found that sufficiently rapid background rotation of either sign acts to strongly stabilize the vortical structure to three-dimensional perturbations.

Our analyses for the rotating stratified Kelvin–Helmholtz wavetrain have shown that the influence of stable stratification on the modes of instability is similar to the effect demonstrated for the non-rotating stratified case, namely that the growth rates of the most unstable modes decrease rapidly as the inverse square of the Froude number rises. The growth rate of the E_0 edge mode, which is the dominant mode in the unstratified case, decreases most dramatically with Fr^{-2}. The E_1 edge mode, however, stabilizes much more slowly and, therefore, becomes the dominant mode in the spectrum of anticyclonic vortices for slow background rotation. The elliptical ϵ mode is the least affected by stable stratification and starts to play a crucial role in the vicinity of $Ro^{-1} = 0.3$. This result is extremely important insofar as the applicability of our theory to the understanding of a number of applications in geophysically interesting circumstances is concerned. Consider, in particular, the interesting observation that the anticyclonic vortices that one would expect to observe in the von Kármán vortex street that is often seen in satellite images of the flow in the lee of oceanic islands are often absent, as illustrated in figure 1(b). If, as we suggest might on occasion be the case, the destruction of the anticyclonic columns could be due to the edge mode, it is clearly important that the mode survives in the presence of finite density stratification parallel to the axis of the vortex tubes. It is also

important that sufficiently strong density stratification will suppress the destruction of anticyclones, thus allowing the existence of a complete von Kármán street, as is also observed (see figure 1a).

The final aspect of the coherent structure destruction mechanisms analysed herein has involved an investigation of the influence of the background vorticity distribution in the vortices as well as the ellipticity of the vortex itself on the stability characteristics of vortex tubes in rotating unstratified and rotating stratified environments. In order to investigate these issues, we have employed a model which is similar to the Kida model as basic-state vorticity distribution in the three-dimensional linear stability analysis. Two different cases were analysed in detail, namely the case of the elliptical Kida-like model vortex with the ellipticity set equal to the ellipticity of the time-averaged vorticity field for the post-pairing phase of the Kelvin–Helmholtz shear flow and the circular limit of the elliptical Kida-like model. Through analyses of the former case we demonstrated that the details of the vorticity distribution in an elliptical vortex do not significantly influence its stability characteristics. Through the analysis of stability of the circular limit of the Kida-like model we showed that even the ellipticity itself does not significantly influence the stability characteristics of the coherent structure, except over the limited range of background rotation in the vicinity of $Ro^{-1} = 0.3$ where a new elliptical mechanism of instability exists. This branch of unstable modes has not previously been identified. Our analyses of the rotating and stratified cases of the above vorticity distributions have demonstrated that instability spectra for the elliptical and the circular vortices are very similar to the spectra for the Kelvin–Helmholtz vortex. We therefore expect the main features of our results to carry over directly to the understanding of a variety of geophysical circumstances in which, at moderately large Rossby numbers ($Ro > 1$), anticyclonic vortex columns might be expected but are nevertheless not observed. Probably the most important of these circumstances concerns the above-mentioned asymmetry that is often seen to characterize the von Kármán vortex street that forms in the atmosphere in flows over and around oceanic islands. The anticyclonic elements of the street are often absent and the Rossby number characteristic of the environment is, indeed, moderately high. Our estimation of the inverse Rossby number for the von Kármán vortex street presented in figure 1 gives $1/Ro = 0.27$–0.45. It should be noted that these values of the Rossby number are very close to the most unstable region in the spectra presented in figure 14. The existence of this broken symmetry associated with the selective destruction of anticyclones at moderate Rossby number has also been very clearly revealed in the numerical simulation of stratified rotating turbulence reported by Bartello *et al.* (1994).

By way of final comment it is also important to note that we have made no explicit effort here to connect our results on the stability of columnar vortices at moderate Rossby number to the recent results of Dritschel & de la Torre Juarez (1996) for the same stability problem at very small Rossby number in which regime the quasi-geostrophic approximation may be valid (e.g. Pedlosky 1987). The fact that these authors find instability to persist into this regime suggests that it should prove interesting to extend the work discussed herein to explore the asymptotic properties of the solution for $Ro \ll 1$. Such analyses will be described elsewhere.

Appendix

Explicit mathematical expressions for the four-dimensional coefficient arrays that appear in equations (2.15), (2.17) and (2.18) are as follows:

$$(1+\delta_{\mu 0})\langle UU\rangle^{k\mu}_{\lambda v} = -i\lambda\alpha\langle F^*_{k\mu}\tilde{U}F_{\lambda v}\rangle - \langle F^*_{k\mu}\tilde{U}_x F_{\lambda v}\rangle + D_v\langle F^*_{k\mu}\tilde{W}G_{\lambda v}\rangle + \frac{ik\alpha D_v}{RoA_{k\mu}}\langle F^*_{k\mu}G_{\lambda v}\rangle$$

$$+2\frac{\lambda k\alpha^2}{A_{k\mu}}\langle F^*_{k\mu}\tilde{U}_x F_{\lambda v}\rangle + 2\frac{ik\alpha D_v}{A_{k\mu}}\langle F^*_{k\mu}\tilde{W}_x G_{\lambda v}\rangle - \frac{1}{Re}A_{\lambda v}\delta_{k\lambda}\delta_{\mu v}(1+\delta_{\mu 0}),$$

$$(1+\delta_{\mu 0})\langle UW\rangle^{k\mu}_{\lambda v} = -\langle F^*_{k\mu}\tilde{U}_z G_{\lambda v}\rangle - \frac{\lambda k\alpha^2}{RoA_{k\mu}}\langle F^*_{k\mu}G_{\lambda v}\rangle$$

$$+2\frac{\lambda k\alpha^2}{A_{k\mu}}\langle F^*_{k\mu}\tilde{U}_z G_{\lambda v}\rangle - 2\frac{ik\alpha D_v}{A_{k\mu}}\langle F^*_{k\mu}\tilde{W}_z F_{\lambda v}\rangle + \frac{1}{Ro}\langle F^*_{k\mu}G_{\lambda v}\rangle,$$

$$(1+\delta_{\mu 0})\langle U\rho\rangle^{k\mu}_{\lambda v} = -\frac{dk\alpha}{Fr^2 A_{k\mu}}\langle F^*_{k\mu}G_{\lambda v}\rangle,$$

$$(1+\delta_{\mu 0})\langle VU\rangle^{k\mu}_{\lambda v} = \frac{idD_v}{RoA_{k\mu}}\langle F^*_{k\mu}G_{\lambda v}\rangle + \frac{2d\lambda\alpha}{A_{k\mu}}\langle F^*_{k\mu}\tilde{U}_x F_{\lambda v}\rangle + \frac{2idD_v}{A_{k\mu}}\langle F^*_{k\mu}\tilde{W}_x G_{\lambda v}\rangle,$$

$$(1+\delta_{\mu 0})\langle VV\rangle^{k\mu}_{\lambda v} = -i\lambda\alpha\langle F^*_{k\mu}\tilde{U}F_{\lambda v}\rangle + D_v\langle F^*_{k\mu}\tilde{W}G_{\lambda v}\rangle - \frac{A_{\lambda v}}{Re}\delta_{k\lambda}\delta_{\mu v}(1+\delta_{\mu 0}),$$

$$(1+\delta_{\mu 0})\langle VW\rangle^{k\mu}_{\lambda v} = -\frac{d\lambda\alpha}{RoA_{k\mu}}\langle F^*_{k\mu}G_{\lambda v}\rangle + \frac{2d\lambda\alpha}{A_{k\mu}}\langle F^*_{k\mu}\tilde{U}_z F_{\lambda v}\rangle - \frac{2idD_v}{A_{k\mu}}\langle F^*_{k\mu}\tilde{W}_z F_{\lambda v}\rangle,$$

$$(1+\delta_{\mu 0})\langle V\rho\rangle^{k\mu}_{\lambda v} = \frac{1}{Fr^2}\left(1-\frac{d^2}{A_{k\mu}}\right)\langle F^*_{k\mu}G_{\lambda v}\rangle,$$

$$\langle WU\rangle^{k\mu}_{\lambda v} = -\langle G^*_{k\mu}\tilde{W}_x F_{\lambda v}\rangle - \frac{D_v D_\mu}{RoA_{k\mu}}\langle F^*_{k\mu}G_{\lambda v}\rangle$$

$$+\frac{2i\lambda\alpha D_\mu}{A_{k\mu}}\langle F^*_{k\mu}\tilde{U}_x F_{\lambda v}\rangle - \frac{2D_v D_\mu}{A_{k\mu}}\langle F^*_{k\mu}\tilde{W}_x G_{\lambda v}\rangle - \frac{1}{Ro}\langle G^*_{k\mu}F_{\lambda v}\rangle,$$

$$\langle WW\rangle^{k\mu}_{\lambda v} = -i\lambda\alpha\langle G^*_{k\mu}\tilde{U}G_{\lambda v}\rangle - D_v\langle G^*_{k\mu}\tilde{W}F_{\lambda v}\rangle - \langle G^*_{k\mu}\tilde{W}_z G_{\lambda v}\rangle - \frac{i\lambda\alpha D_\mu}{RoA_{k\mu}}\langle F^*_{k\mu}G_{\lambda v}\rangle$$

$$+2\frac{i\lambda\alpha D_\mu}{A_{k\mu}}\langle F^*_{k\mu}\tilde{U}_z F_{\lambda v}\rangle + \frac{2D_\mu D_v}{A_{k\mu}}\langle F^*_{k\mu}\tilde{W}_z F_{\lambda v}\rangle - \frac{1}{Re}A_{\lambda v}\delta_{k\lambda}\delta_{\mu v},$$

$$\langle W\rho\rangle^{k\mu}_{\lambda v} = -\frac{idD_\mu}{Fr^2 A_{k\mu}}\langle F^*_{k\mu}G_{\lambda v}\rangle,$$

$$\langle\rho U\rangle^{k\mu}_{\lambda v} = \frac{\lambda\alpha}{d}\langle G^*_{k\mu}F_{\lambda v}\rangle,$$

$$\langle\rho V\rangle^{k\mu}_{\lambda v} = -\langle G^*_{k\mu}F_{\lambda v}\rangle,$$

$$\langle\rho W\rangle^{k\mu}_{\lambda v} = -\frac{iD_v}{d}\langle G^*_{k\mu}F_{\lambda v}\rangle,$$

$$\langle\rho\rho\rangle^{k\mu}_{\lambda v} = -D_v\langle G^*_{k\mu}\tilde{W}F_{\lambda v}\rangle - i\lambda\alpha\langle G^*_{k\mu}\tilde{U}G_{\lambda v}\rangle,$$

where

$$\langle\star\rangle = \frac{\alpha}{\pi H}\int_0^{2\pi/\alpha}\mathrm{d}x\int_0^H \star\ \mathrm{d}z,$$

$$D_v = \frac{v\pi}{H},\quad A_{\lambda v} = (\lambda\alpha)^2 + d^2 + D_v^2.$$

REFERENCES

BARTELLO, P., METAIS, O. & LESIEUR, M. 1994 Coherent structures in rotating three-dimensional turbulence. *J. Fluid Mech.* **273**, 1–29.

BAYLY, B. J. 1986 Three-dimensional instability of elliptical flow. *Phys. Rev. Lett.* **57**, 2160–2163.

BAYM, G. 1968 *Lectures on Quantum Mechanics.* W. A. Benjamin.

BROWAND, F. K. & HO, C. M. 1983 The mixing layer: an example of quasi two-dimensional turbulence. *J. Mec. Num. Spec.* 99–120.

CARNEVALE, G. F., BRISCOLINI, M., KLOOSTERZIEL, R. C. & VALLIS, G. K. 1997 Three-dimensionally perturbed vortex tubes in a rotating flow. *J. Fluid Mech.* **341**, 127–163.

CAULFIELD, C. P. & PELTIER W. R. 1994 Three dimensionalization of the stratified mixing layers. *Phys. Fluids* **6**, 3803–3805.

CHANDRASEKHAR, S. 1968 *Hydrodynamic and Hydrodynamic Stability.* Clarendon Press.

CORCOS, G. M. & SHERMAN, F. S. 1984 The mixing layer: deterministic models of a turbulent flow. Part 1. Introduction and the two-dimensional flow. *J. Fluid Mech.* **139**, 29–65.

DRITSCHEL, D. G. & TORRE JUAREZ, M. DE LA 1996 The instability and breakdown of tall columnar vortices in a quasi-geostrophic fluid. *J. Fluid Mech.* **328**, 129–160.

GREENSPAN, H. P. 1968 *The Theory of Rotating Fluids.* Cambridge University Press.

KELLY, R. E. 1967 On the stability of an inviscid shear layer which is periodic in space and time. *J. Fluid Mech.* **27**, 657–689.

KIDA, S. 1981 Motion of an elliptic vortex in a uniform shear flow. *J. Phys. Soc. Japan* **50**, 3517–3520.

KLAASSEN, G. P. & PELTIER, W. R. 1985a Evolution of finite amplitude Kelvin–Helmholtz billows in two spatial dimensions. *J. Atmos. Sci.* **42**, 1321–1339.

KLAASSEN, G. P. & PELTIER, W. R. 1985b The onset of turbulence in finite-amplitude Kelvin–Helmholtz billows. *J. Fluid Mech.* **155**, 1–35.

KLAASSEN, G. P. & PELTIER, W. R. 1989 The role of transverse secondary instabilities in the evolution of the shear layers. *J. Fluid Mech.* **202**, 367–402.

KLAASSEN, G. P. & PELTIER, W. R. 1991 The influence of stratification on secondary instability in free shear layers. *J. Fluid Mech.* **227**, 71–106.

KLOOSTERZIEL, R. C. & HEIJST, G. J. F. VAN 1991 An experimental study of unstable barotropic vortices in a rotating fluid. *J. Fluid Mech.* **223**, 1–24.

LESIEUR, M., STAQUET, C., LE ROY, P. & COMTE, P. 1988 The mixing layer and its coherence examined from the point of view of two-dimensional turbulence. *J. Fluid Mech.* **192**, 511–534.

MOORE, D. W. & SAFFMAN, P. G. 1971 *Aircraft Wake Turbulence and Its Detection.* Plenum.

PEDLOSKY, J. 1987 *Geophysical Fluid Dynamics.* Springer.

PELTIER, W. R., HALLE, J. & CLARK, T. L. 1978 The evolution of finite amplitude Kelvin–Helmholtz billows. *Geophys. Astrophys. Fluid Dyn.* **10**, 53–87.

PIERREHUMBERT, R. T. & WIDNALL, S. E. 1982 The two- and three-dimensional instabilities of a spatially periodic shear layer. *J. Fluid Mech.* **114**, 59–82.

POLVANI, L. M., WISDOM, J., DEJONG, E. & INGERSOLL, A. P. 1990 Simple dynamic models of Neptune's Great Dark Spot. *Science* **249**, 1393–1398.

SMYTH, W. D. & PELTIER, W. R. 1989 The transition between Kelvin–Helmholtz and Holmboe instability: an investigation of the overreflection hypothesis. *J. Atmos Sci.* **46**, 3698–3720.

SMYTH, W. D. & PELTIER, W. R. 1991 Instability and transition in finite-amplitude Kelvin–Helmholtz and Holmboe waves. *J. Fluid Mech.* **228**, 387–415.

SMYTH, W. D. & PELTIER, W. R. 1993 Two-dimensional turbulence in homogeneous and stratified shear layers. *Geophys. Astrophys. Fluid Dyn.* **69**, 1–32.

SMYTH, W. D. & PELTIER, W. R. 1994 Three-dimensionalization of barotropic vortices on the f-plane. *J. Fluid Mech.* **265**, 25–64.

STUART, J. T. 1967 On finite amplitude oscillations in laminar mixing layers. *J. Fluid Mech.* **29**, 417–440.

WALEFFE, F. 1990 On the three-dimensional instability of strained vortices. *Phys. Fluids* A **2**, 76–80.

WYGNANSKI, I., OSTER, D., FIEDLER, H. & DZIOMBA, B. 1979 On the perseverance of quasi-two-dimensional eddy structures in a turbulent mixing layer. *J. Fluid Mech.* **93**, 325–335.